UNIVERSIDADE DE BRASÍLIA
Faculdade de Tecnologia
Departamento de Engenharia Mecânica

GRADUATION PROJECT

NUMERICAL SIMULATION AND VALIDATION OF THE AEROACOUSTIC FLOW FIELD RESULTING FROM GUST-AIRFOIL INTERACTION

BY
Rafael Lobo Bites Leão

Report submitted as partial requirement for obtaining the degree of Mechanical Engineer.

Examination Committee

Prof. Roberto Francisco Bobenrieth Miserda, UnB/ENM

Prof. Gustavo Coelho Abade, UnB/ENM

Prof. Rafael Gabler Gontijo, UnB/ENM

Brasília, 28th of june, 2011.

ACKNOWLEDGMENTS

Gostaria de agradecer primeiramente o Laboratório de aeroacústica computacional - CAALab em especial Braulio e Ana. Agradeco também à Equipe Calango Alado de AeroDesign. Esse grupo fez o melhor AeroDesign que eu já vi, e aquele ano de trabalho me ensinou engenharia, trabalho em grupo e deu ae presente meus melhores amigos. Esse trabalho e todos os outros que vierem pela frente são gracas a minha família: Seu Arquiarino, Dona Divina, Maninho, Juju, Marcão, Mateus e, mais recentemente, Maria Luisa. Valeu pelo apoio pessoal. Professor Roberto, sua paciência e perseverânça são inspiradoras. Obrigado por acreditar no meu trabalho. Mari, você que está sempre do meu lado, obrigado.

Contents

1 INTRODUCTION **1**

1.1 Work Frame 1

1.2 Work Purposes 1

1.3 Work Placement 1

1.3.1 general aspects 2

2 AIRCRAFT NOISE SOURCES **7**

2.1 Airframe noise 7

2.2 Airfoils self-noise mechanism 8

3 BIBLIOGRAFIC REVIEW **9**

3.1 Works on vortical gust response 9

3.2 Bibliografic Review on self-induced noise 11

4 AIRFOIL-GUST INTERACTION BENCHMARK **15**

4.1 Benchmark Setup 15

4.2 Geometry: the joukowski airfoils 18

4.3 Geometry details 19

5 GOVERNING EQUATIONS **21**

5.1 Numerical Method 25

5.2 Immersed-Boundary Technique 32

6 NUMERICAL SIMULATIONS **36**

6.1 Vat-parameters 36

6.1.1 Time-step 36

6.1.2 Artificial Viscosity with Pressure Based Sensor 39

6.2 Time-Averaged Flow Solution with Pressure Based Sensor 42

6.3 Time-Averaged Flow Solution with Divergent and Vorticity Sensors . . 46

6.4 Linearized-euler Solutions 49

6.4.1 Vortical gust on uniform flow field 49

6.4.2 Airfoil Gust Response 52

7 Conclusion **61**

7.1 Next Steps 64

REFERENCES **65**

ABSTRACT

This work consists of validation of VAT (Virtual Aeroacoustic Tunnel) for a single airfoil vortical gust reponse.

The software used to acquire the simulations results is the Virtual Aeroacoustic Tunnel (VAT), an inhouse code developed by the Computational Aeroacoustics Laboratory of University of Brasília, which obtains the aeroacoustics field by the solutions of Navier-Stokes, Euler or Linearized-Euler equations in its compressible formulation through volume elements discretization.

The work is part of the Silent Aircraft project sponsored by Embraer - Brazilian Aeronautics Enterprise and associated with University of Brasília among others.

Key-Words: Aeroacoustics, single airfoil Noise, Vortical Gust, linearized-euler equations, Numerical Simulation, Immersed Boundary.

List of Figures

1.1 Fourier transform example.(*Basic Principles of Sound and an Introduction to Aircraft Noise* (Embraer)) 4
1.2 monopole - illustration and directivity diagram - figure from *http://www.kettering.edu/ drussell/* 4
1.3 dipole - illustration and directivity diagram - figure from *http://www.kettering.edu/ drussell/* 5
1.4 quadrupole - illustration and directivity diagram - figure from *http://www.kettering.edu/ drussell/* 6

2.1 The most important airframe noise sources 7

3.1 Computational (x,y,t) domain with instantaneus ρv-component of gust, k=1.0. Vladimir *et al* (2004a), ... 10
3.2 left: grid-partitioned computaional domain. Right: grid details near cambered airfoil surface. Vladimir *et al* (2004b), ... 11

4.1 Airfoil in a two-dimensional, periodic gust ($k = 1.0$) (component U_x and U_y separated) 16
4.2 Airfoil in a two-dimensional, periodic gust ($k = 1.0$) 16
4.3 vorticity field imposed by the vortical-gust for $k = 1$ 17
4.4 Airfoil geometry for Case 1 18
4.5 Airfoil geometry for Case 2 19
4.6 Truncaded Trailing edge of Case 1 airfoil 20
4.7 Truncaded Trailing edge of Case 2 airfoil 20

6.1 numeric oscilations due to nonlinearity of eulers equation. The variable plotted is $\beta_T = |\nabla T|^{1/20}$. 37
6.2 instantaneus field of 10^4 iterations for case1. The variable plotted is $\beta_T = |\nabla T|^{1/20}$. 38
6.3 instantaneus field of $62 * 10^4$ iterations for case1, $K^{(2)} = 0.25$ and $K^{(4)} = 1/128$. The variable plotted is $\beta_T = |\nabla T|^{1/20}$. 39
6.4 instantaneus field of $2 * 10^4$ iterations for case1, $K^{(2)} = 0.175$ and $K^{(4)} = 1/128$. The variable plotted is $\beta_T = |\nabla T|^{1/20}$. 40
6.5 instantaneus field of $47 * 10^4$ iterations for case1, $K^{(2)} = 0.5$ and $K^{(4)} = 1/64$. The variable plotted is $\beta_T = |\nabla T|^{1/20}$. 41

6.6 Unsteady flow solution for the nonlinear Euler equations for case1. The variable plotted is $\beta_T = |\nabla T|^{1/20}$. 42
6.7 Unsteady flow solution for the nonlinear Euler equations for case2. The variable plotted is $\beta_T = |\nabla T|^{1/20}$. 43
6.8 pressure probe above the airfoil for case1. 44
6.9 mean pressure probe above the airfoil for case1. 44
6.10 pressure probe above the airfoil for case2. 45
6.11 mean pressure probe above the airfoil for case2. 45
6.12 Unsteady flow solution for the nonlinear Euler equations for case1 with the new sensors implementation. The variable plotted is $\beta_T = |\nabla T|^{1/20}$. 46
6.13 mean c_p field for case 1 47
6.14 mean and instantaneus pressure probes localized under the airfoil for case 1 48
6.15 mean and instantaneus pressure probes localized in the stream for case 1 48
6.16 mean and instantaneus pressure probes localized in the center of domain for uniform flow field for k=1.0 49
6.17 v' field for $k_x = k_y = 0.1$ 50
6.18 mean and instantaneus pressure probes localized in the center of domain for uniform flow field for k=2.0 51
6.19 v' field for $k_x = k_y = 2.0$ 52
6.20 v' field for $k_x = k_y = 1.0$ 53
6.21 v' field for $k_x = k_y = 0.1$ 54
6.22 Acoustic intensity on circle $R = 1C$, Case 1, k=0.1 55
6.23 Acoustic intensity on circle $R = 2C$, Case 1, k=0.1 55
6.24 Acoustic intensity on circle $R = 1C$, Case 1, k=1.0 56
6.25 Acoustic intensity on circle $R = 2C$, Case 1, k=1.0 56
6.26 Acoustic intensity on circle $R = 1C$, Case 1, k=2.0 57
6.27 Acoustic intensity on circle $R = 2C$, Case 1, k=2.0 57
6.28 probe position 58
6.29 probes 03 and 07 pressure signal, Case 1, k=2.0 58
6.30 probes 03 and 05 pressure signal, Case 1, k=2.0 59
6.31 probes 03 pressure signal, Case 1, k=2.0 and k=1.0 60

7.1 acoustic intensity comparation for case 1 k=0.1 r=1.0 61
7.2 acoustic intensity comparation for case 1 k=1.0 r=1.0 62
7.3 acoustic intensity comparation for case 1 k=2.0 r=1.0 62
7.4 probes 03 frequency spectrum, Case 1, k=0.1 63
7.5 probes 03 frequency spectrum, Case 1, k=0.1 63

7.6 probes 03 frequency spectrum, Case 1, k=0.1 64

LIST OF SYMBOLS

LATIN SYMBOLS

a: non-dimensional acceleration.

a^*: acceleration.

C_1: first non-dimensional gas constant for Sutherland formula.

C_2: second non-dimensional gas constant for Sutherland formula.

C_1^*: first gas constant for Sutherland formula.

C_2^*: second gas constant for Sutherland formula.

c: sound velocity.

c_0: temporal mean of sound velocity.

c_p^*: specific heat under constant pressure.

c_p: non-dimensional specific heat under constant pressure.

c_v: non-dimensional specific heat under constant volume.

$\mathcal{D}(\overline{\mathbf{U}})$: artificial dissipation.

$d_{i+1/2}(\overline{\mathbf{U}})$: artificial dissipation at the $(i+1/2)$ control volume face.

$\mathbf{E}$: non-dimensional flux vector.

e: non-dimensional internal energy per unit mass.

e^*: internal energy per unit mass.

e_k: kinetic energy per unit mass.

e_T: non-dimensional total energy per unit mass.

$\mathbf{i}$: unit vector in x direction.

$\mathbf{j}$: unit vector in y direction.

$\mathbf{k}$: unit vector in z direction.

k: non-dimensional thermal conductivity, wave number.

k_∞^*: thermal conductivity of freestream flow

$K^{(2)}$: second order artificial dissipation constant.

$K^{(4)}$: fourth order artificial dissipation constant.

L^*: main length.

$\mathbf{n}$: unit vector normal to the control surface.

p: non-dimensional thermodynamic pressure.

p^*: thermodynamic pressure.

p_0: temporal mean of thermodynamic pressure.

q_s: non-dimensional volumetric flux.

q_i: vector component of heat flux density in **i** direction.

S_{ij}:non-dimensional strain rate tensor.

$(s_x)_{i+1/2}$: non-dimensional vector component of surface in x direction and $(i+1/2)$ position.

$(s_y)_{i+1/2}$: non-dimensional vector component of surface in y direction and $(i+1/2)$ position.

$(s_z)_{i+1/2}$: non-dimensional vector component of surface in z direction and $(i+1/2)$ position..

T: non-dimensional temperature.

T^*: temperature.

T^*_∞: freestream temperature.

t: non-dimensional time coordinate.

t^*: time coordinate.

U: velocity vector modulus.

U: non-dimensional conservative variables vector.

U^*_∞: freestream velocity magnitude.

u: non-dimensional velocity vector component in x direction.

u^*: velocity vector component in x direction.

u: non-dimensional velocity vector.

u_i: non-dimensional velocity vector component in **i** direction.

V: discretized control volume non-dimensional volume.

v: non-dimensional velocity vector component in y direction.

v^*: velocity vector component in y direction.

w: non-dimensional velocity vector component in z direction..

w^*: velocity vector component in z direction..

R^*: gas constant.

$\mathbf{S}_{i+1/2}$: non-dimensional surface vector in $(i+1/2)$ position.

x: first non-dimensional spatial coordinate.

x^*: first spatial coordinate.

x_i: spatial coordinate in **i** direction.

y: second non-dimensional spatial coordinate.

y^*: second spatial coordinate.

z: third non-dimensional spatial coordinate.

z^*: third spatial coordinate.

GREEK SYMBOLS

Δt: non-dimensional time step.

$\Delta\overline{\mathbf{U}}$: non-dimensional variables variation vactor.

δ_{ij}: Kronecker's delta.

ϵ: numerical value to avoid division by zero at Ducros sensor.

$\epsilon^{(2)}$: second order artificial dissipation coefficient..

$\epsilon^{(4)}$: fourth order artificial dissipation coefficient.

Φ: Ducros sensor.

γ: specific heat ratio.

μ: non-dimensional dynamic viscosity.

μ^*: dynamic viscosity.

μ^*_∞: freestream dynamic viscosity.

Π: non-dimensional flux tensor.

ρ: non-dimensional density.

ρ^*: density.

ρ^*_∞: freestream density.

$\tau_{i,j}$: non-dimensional shear stress tensor.

Ψ: Jameson sensor.

NON-DIMENSIONAL NUMBERS

M: Mach number.

Pr: Prandtl number.

Re: Reynolds number.

St: Strouhal number.

ACRONYM

CAA: Computational Aeroacoustics.

CFL: Courant Friedrichs Lewy Number.

rms: Root Mean Square.

SPL: Sound Pressure Level.

VAT: Virtual Aeroacoustic Tunnel.

1 INTRODUCTION

1.1 Work Frame

The work is divided in 7 chapters. The first chapter is the introduction, which includes the work purposes and General aspects.

The second chapter highlights some airframe noise sources, emphasizing self-induced airfoil noise.

The third chapter brings a bibliografic review.

The fourth chapter brings the set of the Airfoil Gust Reponse Problem.

The fifth chapter describes the governing equations, the mathematical model and the numerical method used to obtain the aeroacoustic solution for the proposed problem.

The sixth chapter characterizes the preliminary results obtained for each airofoil simulated, the time-averaged-euler solution for the symmetric airfoil, the gust implementations approaches and the linearzed-euler solutions for the symmetric airfoil.

The seventh chapter presents the work's conclusions and next steps.

1.2 Work Purposes

The major purpose of this work is to study the self-induced noise produced on airfoils interacting with gust using the Virtual Aeroacoustic Tunnel (VAT) developed by the Computational Aeroacoustic laboratory (CaaLab). This work consists of three stages. The first stage consist in a time-averaged solutions of the euler equations to be used as a mean field for a linearized euler solution. The second stage is the gust implementation on the code and the later is to validate the code using the vortical gust airfoil interaction proposed in the NASA "Fourth Computational Aeroacoustic Workshop on Benchmark Problems".

1.3 Work Placement

Air traffic is predicted to grow by 5% per year in the short and medium term. Technology improvements are required to facilitate this growth without unacceptable levels of noise. In this context Embraer and FAPESP created the project Aeronave Silenciosa. The project objective is to research about aircraft noise reduction and noise generation mechanisms. CAALab-UnB (Computacional Aeroacoustic Laboratory) is inserted in this project and the focus is fan noise.

1.3.1 general aspects

1.3.1.1 Aircraft noise and health issues

On a 1997 questionnaire distributed to two groups (one living near a major airport, and the other in a quiet neighborhood) two-thirds of those living near the airport indicated they were bothered by aircraft noise, and most said that it interfered with their daily activities. The same two-thirds complained more than the other group of sleep difficulties, and also perceived themselves as being in poorer health.

Perhaps even more alarming, the European Commission, which governs the European Union (E.U.), considers living near an airport to be a risk factor for coronary heart disease and stroke, as increased blood pressure from noise pollution can trigger these more serious maladies. The E.U. estimates that 20 percent of Europe's population (or about 80 million people) are exposed to airport noise levels it considers unhealthy and unacceptable.

Airport noise can also have negative effects on children's health and development. A 1980 study examining the impact of airport noise on children's health found higher blood pressure in kids living near Los Angeles'LAX airport than in those living farther away. A 1995 German study found a link between chronic noise exposure at Munich's International Airport and elevated nervous system activity and cardiovascular levels in children living nearby. And a 2005 study published in the prestigious British medical journal, The Lancet, found that kids living near airports in Britain, Holland and Spain lagged behind their classmates in reading by two months for every five decibel increase above average noise levels in their surroundings. The study also associated aircraft noise with lowered reading comprehension, even after socio-economic differences were considered. *website (1)*,

1.3.1.2 Some Acoustic Definitions

The sound pressure level, eq 1.1, is a logarithmic measure of the square root of the mean squared - rms of the acoustic pressure fluctuation - $p'_{(rms)}$ relative to a refference value.

$$SPL = 20log10\left(\frac{p'_{rms}}{p_{ref}}\right) \; where \; p_{ref} = 2.10^{-5} \; in \; air \tag{1.1}$$

The sound intensity I is defined as the energy flux (power per surface area) corresponding to sound propagation. The Intensity Level (IL) is given by eq 1.2

$$IL = 10log10\left(\frac{I}{10^{-12}}\frac{W}{m^2}\right) \tag{1.2}$$

The reference pressure level in air $p_{ref} = 2.10^{-5}$Pa correspond to the threshold of hearing at 1kHz for a typical human ear. The reference intensity level $I_{ref} = 10^{-12}\frac{W}{m^2}$ is related to this $p_{ref} = 2.10^{-5}$Pa in air by the relationship valid for prograssive plane waves:

$$I = \frac{p'^2_{rms}}{\rho_0 c_0} \tag{1.3}$$

where $\rho_0 c_0 = 4.10^2 \frac{kg}{m^2 s}$ for air under atmospheric conditions.

An important aspect of acoustics is the frequency analysis of a acoustic spectrum. The acoustic spectrum can be obtained by the Fourier transform given by eq. 1.4.

$$F(w) = \int_{-\infty}^{\infty} f(t)e^{-iwt}\,dt, \; i^2 = -1 \tag{1.4}$$

where $F(w)$ is the complex amplitude, $f(t)$ is the function to be transformed, t is the variable and w the angular frequency.

The sound signal resulted of a numeric simulation are discrete. The Fourier transform in the discrete form is given by eq. 1.5

$$x_k = \frac{1}{n}\sum_{j=0}^{n-1} f_j e^{\frac{2\pi i}{n}jk}, \; k = 0, 1, 2, ..., n-1 \tag{1.5}$$

In this way, the acoustic signal without treatment is transformed from the time domain to the frequency domain by the fourier transform. Figure 1.1 shows an example of the Fourier transform. Figure 1.1-a shows a sine fuction and the respect frequency spectrum. Figure 1.1-b shows a signal with multiple frequencies and the respect frequency spectrum.

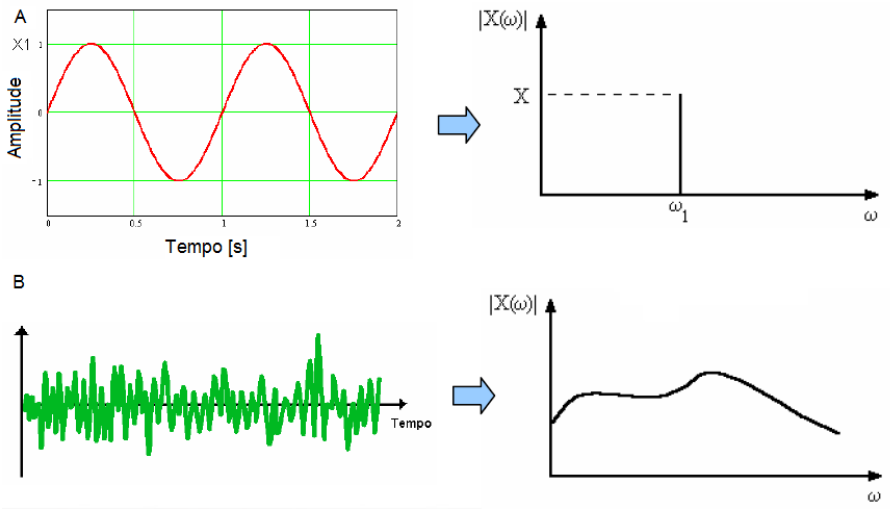

Figure 1.1: Fourier transform example.(*Basic Principles of Sound and an Introduction to Aircraft Noise* (Embraer))

In figure 1.1 is possible to define two basic types of noise: tonal noise and broadband noise. The tonal is characterized by a dominant frequency. The broadband noise does not have a dominant frequency and the spectrum is diffuse in a frequency range.

1.3.1.3 Sound Fields Radiated by Simple Sources

A monopole is a source which radiates sound equally well in all directions. The simplest example of a monopole source would be a sphere whose radius alternately expands and contracts sinusoidally. The monopole source creates a sound wave by alternately introducing and removing fluid into the surrounding area. A boxed loudspeaker at low frequencies acts as a monopole. The directivity pattern for a monopole source is shown in the figure 1.2.

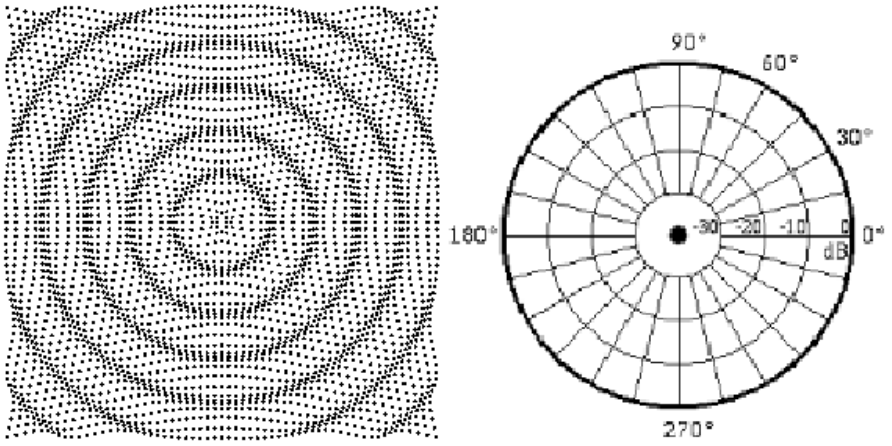

Figure 1.2: monopole - illustration and directivity diagram - figure from *http://www.kettering.edu/ drussell/*

A dipole source consists of two monopole sources of equal strength but opposite phase and separated by a small distance compared with the wavelength of sound. While one source expands the other source contracts. The result is that the fluid (air) near the two sources sloshes back and forth to produce the sound. A sphere which oscillates back and forth acts like a dipole source, as does an unboxed loudspeaker (while the front is pushing outwards the back is sucking in). A dipole source does not radiate sound in all directions equally. The directivity pattern shown in figure 1.3; there are two regions where sound is radiated very well, and two regions where sound cancels.

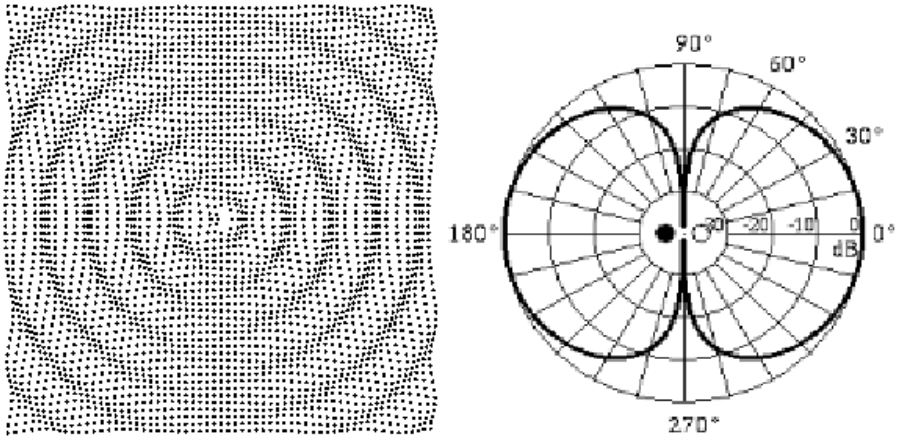

Figure 1.3: dipole - illustration and directivity diagram - figure from *http://www.kettering.edu/ drussell/*

If two opposite phase monopoles make up a dipole, then two opposite dipoles make up a quadrupole source. In a Lateral Quadrupole arrangement the two dipoles do not lie along the same line (four monopoles with alternating phase at the corners of a square). The directivity pattern for a lateral quadrupole looks like a clover-leaf pattern; sound is radiated well in front of each monopole source, but sound is canceled at points equidistant from adjacent opposite monopoles.

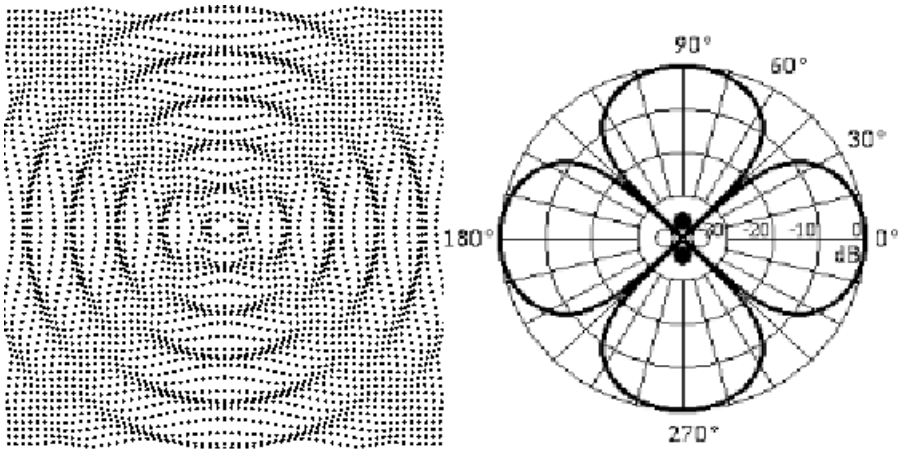

Figure 1.4: quadrupole - illustration and directivity diagram - figure from *http://www.kettering.edu/ drussell/*

2 AIRCRAFT NOISE SOURCES

This chapter describes categories of noise sources in aircrafts with emphasis on airfoil noise.

2.1 Airframe noise

Airframe noise used to considered as the lower limit of aircraft noise. During take-off, engine noise still dominates over airframe noise, but during approach and landing, the noise leves of modern aircraft engines with large bypass ratios have been reduced so much that airframe noise and engine noise are of comparable levels.

Figure 2.1: The most important airframe noise sources

Airframe noise is generated by aerodynamic sound sources that become active when a structure interacts with a flow. The sources can generate tones, e.g. by vortex shedding from cylindrical stays of a landing gear, or broad band noise, like the turbulent boundary layer on the fuselage. The Sources can be small, like a resonating cavity, or they can have large extent, like the flaps mounted upstream of a wing. This large range of scales and source mechanisms makes the study of airframe noise so difficult. Airframe noise levels are directly linked to the aircraft flight speed, so for the design of new aircraft, the key to lower noise levels is to ensure low landing speed. A very good introduction to the subject and an overview of the development of airframe noise research since the 1970s is given by Dobrzynski (2010)

Airframe noise is generally dominated by the noise of the landing gear and the high-lift devices. Cavity tones play an important role on some aircraft although these

tones can almost always be eliminated. Usually, airframe noise sources rank in the order: landing gears, slotted slats, flap and slat side edges, flap and slat tracks, spoilers, followed by interaction sources, e.g. landing gear wake and flap interaction (*Dobrzynski (2010)*). Usually, for short range aircraft with single aisles, the landing gears and high-lift devices contribute more or less equally, while for large, long range and wide body aircraft twin aisles, the dominating airframe noise sources are located in the landing gears.

2.2 Airfoils self-noise mechanism

Airfoil self-noise mechanism is a first effort to understand aerodynamic noise generation. Brooks *et al* (1989), define Airfoil Self-noise as a interaction between an airfoil blade and the turbulence produced in its own boundary layer and near wake. Brooks *et al* (1989), highlights 5 self-noise mechanism. *Turbulent-Boundary-Layer-Trailing-Edge-Noise (TBL-TE)*, *Separation-Stall Noise*, *Laminar-Boundary-Layer-Vortex-Shedding (LBL-VS) Noise*, *Tip Vortex Formation Noise* and *Trailing-Edge-Bluntness-Vortex-Shedding Noise*. At high Reynolds number Re, Turbulent Boundary Layer develop over most of the airfoil. Noise is produced as this turbulence passes over the Trailing edge. At low Reynolds number, largely laminar boundary layers develop, whose instabilities result in vortex shedding and associated noise from the trailing edge. Cunha (2009) suggest a correlation between the stream topology and the Laminar-Boundary-Layer-Vortex-Shedding noise. For nonzero angles of attack, the flow can detach near the TE on the suction sideof the airfoil to produce TE noise due to the shed turbulent vorticity. At very high angles of attack, the separeted flow near the TE gives way to large-scale saparation (deep stall) causing the airfoil to radiate low-frequency noise similar to that of a bluff body in flow. Pimenta and Vizioli (2009) suggest that in an airfoil cascade in off-design conditions (high angles of attack) the noise mechanism is due to this large-scale saparations. For a blunt TE the vortex shedding occur in the small separeted flow region aft TE and it is a source of noise. The remaining source considered by Brooks *et al* (1989), is due to the formation of the tip vortex, containing highly turbulent flow, occuring near the tips of lifting blades of wings.

3 BIBLIOGRAFIC REVIEW

This chapter shows a resume about the works on vortical gust presented in the "Fourth Computational Aeroacoustic Workshop on Benchmark Problems"and a breaf bibliografic review about self-induced noise on airfoils.

3.1 Works on vortical gust response

Scott(2004) proposed a Benchmark problem to test the ability of a CFD/CAA code to accurately predict the unsteady aerodynamic and aeroacoustic reponse of a single airfoil to a two-dimensional, periodic vortical gust.

About this benchmark Wang *et al* (2004), Vladimir *et al* (2004a), and Vladimir *et al* (2004b), contributed in the workshop and proposed different numerical methods to predict the gust response.

Wang *et al* (2004), used the method of space-time conservation element and solution element (abbreviated as the CE/SE method). This method is a finite volume method with second-order accuracy in both space and time. The flux conservation is enforced in both space and time instead of space only. It has low numerical dissipation and disparsion errors. It uses simple non-reflecting boundary conditions and is compatible with unstructured meshes. Wang *et al* (2004), compared results with GUST3D (a frequency-domain solver) and DSEM (a time-domain high-order Discontinuous Spectra Element Method). Comparisons with GUST3D showed good agreement for lower frequencies and comparisons with DSEM the good agreement occur for these higher frequencies.

Vladimir *et al* (2004a), argues that the CAA codes have been developed to accurately capture transient flow behavior by combining a high-accuray spatial differencing scheme with an optimized time-marching method. Thus, any unsteady problem is a transient problem that requires high time accuracy throughout the calculation process. For Vladimir *et al* (2004a), the gust-airfoil interaction problem is an example of a periodic problem, where the exact transient solution starting from the initial conditions may not be of interest. So, the long-term periodic solution is usually the desired output, with the excessive accuracy of the transient calculations being redundant. This view does not match with cases of validation of codes that can solve problem that are non-periodic, but is interesting if the interest is periodic problems.

Vladimir *et al* (2004a), uses the STMA approach proposed by Hixon (2003). In this work the unsteady marching problem in two spatial dimensions is transformed into a steady-state iteractive problem in three dimensions (see figure 3.1). At the same time,

the highly convergent iterative methods from classical CFD can be apllied, increasing accuracy (by using better time derivatives), reducing CPU time (because of less grid points in space-time as well as improved iterative methods), and increasing the parallel performance of the codes (through larger block volumes on each processor and reduced synchronization needs during the iterative proces).

For Vladimir *et al* (2004a), in application to the unsteady gust-airfoil interaction problem, the periodic nature of the flow can be further used to minimize the computational time and effort required to solve the test cases. In particular, the mesh is designed to cover one period of the vortical gust in the time direction, with a periodic boundary condition applied at the time inflow and time outflow boundaries. The STMA solves the nonlinear Euler equations. A iterative method is used to solve the Governing Equations in conservative form. The results for lower frequencies used a mesh of 433*125*17 and for the higher frequency 605*240*17. Even for the higher frequency (finer mesh) the gust was not well solved in the far field regins, which contributed to some inaccuracy in the acoustic derectivity prediction in the far field.

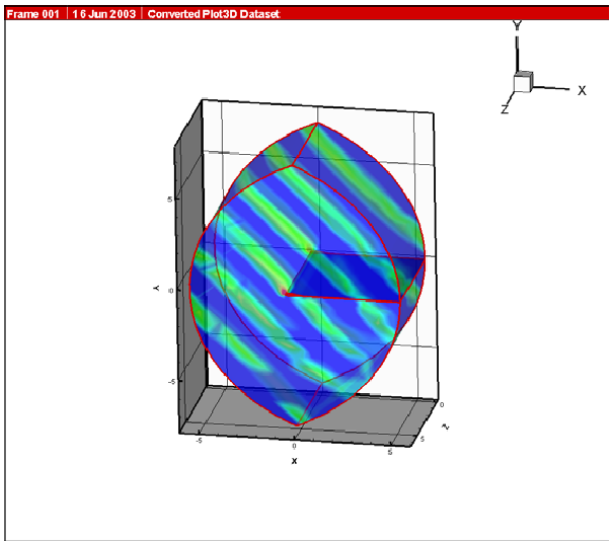

Figure 3.1: Computational (x,y,t) domain with instantaneus ρv-component of gust, k=1.0. Vladimir *et al* (2004a),

Vladimir *et al* (2004b), uses a numerical formulation that employs the low-storage 4^{th} order 5-6 Low Dispersion and Dissipation Runge-Kutta scheme for time marching, and the prefactored 6^{th} order compact scheme and explicit boundary stencils for derivatives. Most of results reported below were obtained from an older prefactored code that used the 10^{th} order explicit filtering at every stage of the Runge-Kutta solver to provide dissipation. A C-grid 2D topology (see figure 3.2) is used to generate grids for both cases of symmetric and cambered Joukowski airfoil, with the grid extending at least 10 chords away from the surface in each direction. Algebraic clustering around

the airfoil in the normal direction and near the trailing edge with streching ratio of 1.05 was used to compound the grid. Some oscilations and loss of accuracy are observed in numerical results near the trailing edge due to the singularity treatment i the grid topology. a careful clustering of grid points near the trailing edge helps to keep these effects localized, with minimal impact on the overall solution. The Vladimir *et al* (2004b), results showed good directivity response for the symmetric airfoil, though for the cambered airfoil the results suffered significantly from the poor gust resolution in the corner regions of the domain and the results for the higher frequency was not even showed.

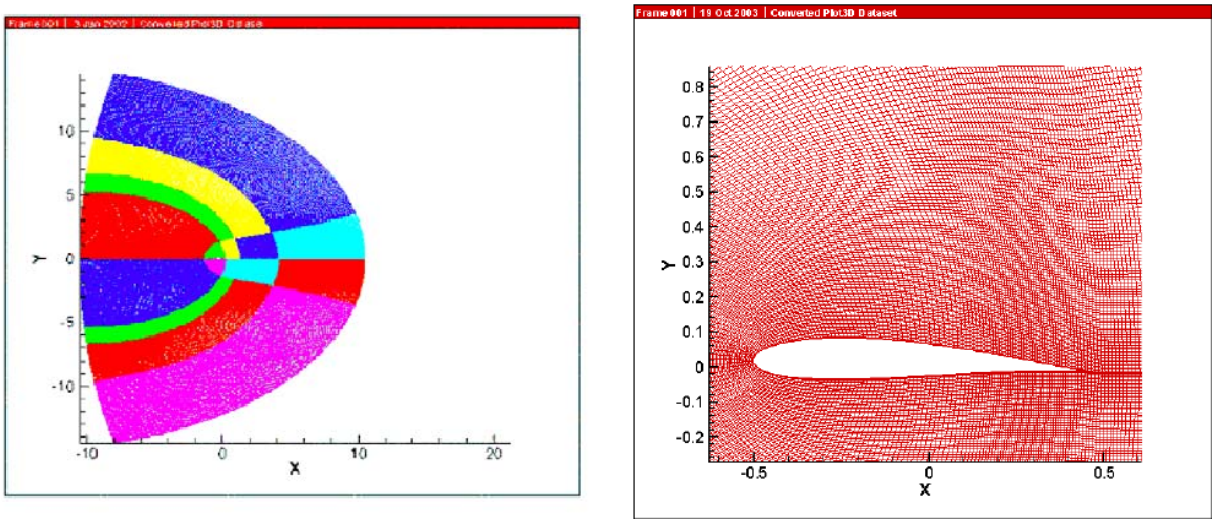

Figure 3.2: left: grid-partitioned computaional domain. Right: grid details near cambered airfoil surface. Vladimir *et al* (2004b),

3.2 Bibliografic Review on self-induced noise

About self induced noise on airfoil the first important contribution on experimental data is attributed to Paterson *et al* (1972), . An experiment in a low turbulence intensity (0,1%) open-jet wind tunnel located in an anechoic chamber was conducted. The far-field acoustic pressure fluctuation was measured as well as the airfoil surface pressure fluctuation on NACA 0012 and NACA 0018 two-dimensional airfoils. The characterization of the vortex shedding for a typical helicopter rotor section through measurements of both surface and far-field acoustics pressure fluctuations was the major objective of the experiment.

Paterson *et al* (1972), concluded that tonal noise was observed in low and moderate Reynolds numbers and was caused by the vortex shedding on the trailing edge. It was observed that a laminar boundary layer on the suction side of the airfoil is a required factor in order to generate tonal noise. Therefore if it is turbulent no tonal noise is

observed. The experimental results provided a well defined description of the ladder-type pattern of the tonal frequency related to the velocity. Morevoer, an expression for the frequency of the main tone as a function of the Strouhal based velocity was proposed. Finally, it was also observed that the nature of the tone was a dipole located near the trailing edge of the airfoil.

Tam (1974) proposed a feedback mechanism to explain the ladder-type structure and concluded that the vortex shedding mechanism is inappropriate to justify the tonal noise generation. Tam (1974) used the data from Paterson *et al* (1972), experiments and made a stability analysis to formulate a theory which illustrates that the tonal noise is actually generated by the feedback loop. The loop consists of an unstable laminar boundary layer on the pressure side of the airfoil that meets the boundary layer on the suction side at the trailing edge and an unstable wake is formed. The wake disturbances are amplified as they propagates donwstream. This oscillatory movement induces the emission of acoustic waves. The feedback loop is completed as the acoustic waves meet the trailing edge and new disturbances are introduced in the wake. Therefore, it was concluded that the self-excited feedback loop is consistent with the presence of a laminar boundary layer on the pressure side of the airfoil, as observed by Paterson *et al* (1972), . It is also explained the reason why the frequency of discrete tones increases with the velocity. The presence of multiple frequencies observed by Paterson *et al* (1972), implies that more than one unstable wave's modes are excited. The dipole nature of the noise is explained by the oscillation of the wake which generates the sound near the airfoil trailing edge . Finally, Tam (1974) proposed an expression to the discrete frequencies which considers the ladder-type pattern of the tonal frequency.

Nash *et al* (1999), conducted an extensive work to investigate the trailing-edge noise generation mechanism. The results suggest that on an acoustic lining environment the ladder-type structure of discrete frequencies disappears. LDA measurements reveal high instabilities on the boundary layer near the trailing edge on the pressure side of the airfoil. Visualizations show that these instabilities roll up to form a regular wake, which is shed in the same frequency of the tonal noise. The presence of instabilities and the acoustic field has a straight correlation with the separated flow on the pressure side of the airfoil and the unsteady Kutta condition is not satisfied. The stability analysis shows that the tonal noise main frequency and the frequency of the most amplified boundary layer instability are the same. Nash *et al* (1999), proposed a new trailing-edge noise generation mechanism. An adverse pressure gradient on the pressure side of the airfoil generates a region which has a point of inflection and the flow is completely separated near the trailing edge. The massively amplification of the T-S waves occurs in this region. Therefore the instabilities roll up into a vortex. The interaction between

the instabilities and the trailing edge results in an oscillatory field that spreads all over the airfoil and vibrates at the same frequency of the most amplified instabilities.

A recent experimental study was performed by Chong *et al* (2009), . This work elucidates the feedback-loop and reaffirms some important features of the trailing edge noise proposed by others investigators. A NACA 0012 airfoil in a low turbulence intensity (0,1% for a Mach number of 0.3) in a open jet wind tunnel placed on anechoic chamber (8m $\times$ 8m $\times$ 8m) experiment was conducted. In order to predict the beginning and the end of the boundary layer separation XFOIL code was used.

Chong *et al* (2009), concluded that the shear layer of the separated region, acting as the amplifier of the incoming T-S wave, is responsible for the noise scattering at the trailing edge. The noise spectrum comprises a broadband hump, embedded with multiples discrete tones. When the T-S waves are scattered into noise, the main frequency is expected to be the characteristic frequency of the instability. An inflection velocity profile of the trailing edge boundary layer is required to occur the noise radiation by the scattering of aerodynamic disturbance.

Measurements of unsteady surface pressure were perfomed with an instrumented NACA 0015 airfoil by Larssen and Devenport (1999) in the Virginia Tech Stability Wind Tunnel. This facilitiy test section has 7.32 m long with a 1.83 m-square cross section. At 30m/s, flow through the empty test section is virtually uniform and of low turbulence intensity ($< 0.05\%$). Background noise levels are acceptable for the aerodynamic measureemnts of interest. Measurements of this work were made at $Re = 1.17 \cdot 10^6$ with the airfoil at zero angle of attack. a square bi-planar grid is mounted 5.82 m upstream of the airfoil leading edge. This grid generates a turbulence with a streamwise integral lengthscale $\lambda = 8.18cm$ to result in a turbulence intensity of 3.93% at 30 m/s. The airfoil is instrumented with an array os 96 microphones, embedded in the upper and lower airfoil surfaces over the center of its span.

Casper and Farassat (2002) uses an analytic result in acoustic called "Formulation 1B" proposed by Farassat to compute broadband trailing edge noise from an unsteady surface pressure distribution on a thin airfoil in the time-domain. This formulation is a solution of the Fowcs Williams-Hawkings equation with the loading source term. The results are compared to analytical results and experimental measurements. Good agreement between predictions and measurements is obtained. Casper and Farassat (2002) argues that any successful broadband loading noise prediction requires an understanding of two physical process: the character of the time-dependent surface pressure that provides the acoustic source, and the manner in wich that source gives rise to an acoustic signal. Casper and Farassat (2002) are advocates of the use of time domain methods in the prediction of broadband noise because of the decoupling of the aerody-

namics from the acoustic. For Casper and Farassat (2002) the chief advantages of time domain methods is their potential for direct use of time-dependent surface pressure statistics from experiments or computer simulations.

4 AIRFOIL-GUST INTERACTION BENCHMARK

Most unsteady aerodynamic and aeroacoustic analyses considering interaction of upstream flow nonuniformities with downstream structural components follow linear theory wherein the unteady part of the flow is considered a small pertubation about the steady mean flowfield, Crivellini *et al*(2002), . This approach relies on solutions to the linearized Euler equations and is used to understand problems like the rotor-stator interaction.

The single airfoil gust reponse problem was proposed in the fourth CAA workshop on benchmark problems in order to assess the capacity of a numerical methodology in handling the generation and propagation of sound waves in the presence of complex geometries with no dispersion or dissipation. The fourth CAA workshop emphasizes the apllication of CAA methods to the solution of realistc problems. In this focus a pratical application of CAA for computing noise generated by turbomachinery involves the modeling of the noise source mechanism as a vortical gust interacting with an airfoil.

4.1 Benchmark Setup

The upstream velocity is

$$\vec{U} = U_\infty \vec{i} + \vec{a} cos[\vec{k} - \vec{i} U_\infty t] \tag{4.1}$$

where $\vec{x} = (x, y)$ denotes the spatial coordinates, $\vec{a} = (a_x, a_y)$ is the gust amplitude vector with $a_x = -\epsilon U_\infty k_y/|\vec{k}|$, $a_y = \epsilon U_\infty k_x/|\vec{k}|$, $\vec{k}$ is the wave number vector, and ϵ is a small parameter satisfying $\epsilon \ll 1$

The x component of the upstream velocity is

$$U_x = U_\infty + a_x cos[(x - U_\infty t)k_x + y k_y] \tag{4.2}$$

The y component of the upstream velocity is

$$U_y = a_y cos[(x - U_\infty t)k_x + y k_y] \tag{4.3}$$

Figure 4.1 and 4.2 illustrate the gust with vector that represents the upstream velocity variation. Figure 4.1 shows the isolated components $\vec{U}$ where U_x gust component is shown in lines in y direction and U_y gust component is shown in lines in x direction. Figure 4.2 shows the vortical-gust vector with the two components for multiple points of the field.

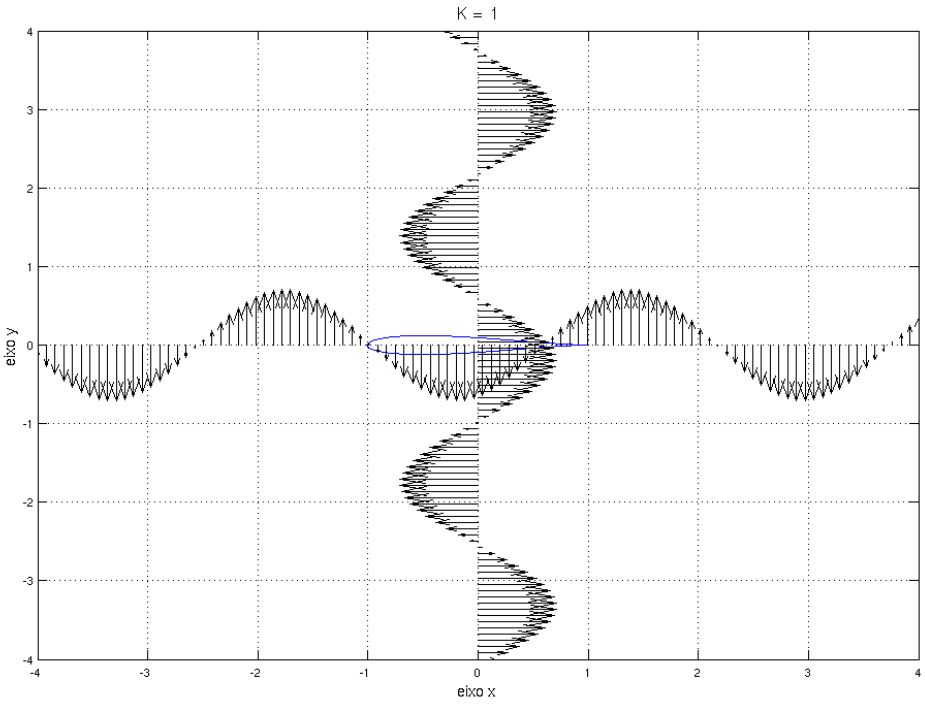

Figure 4.1: Airfoil in a two-dimensional, periodic gust ($k = 1.0$) (component U_x and U_y separated)

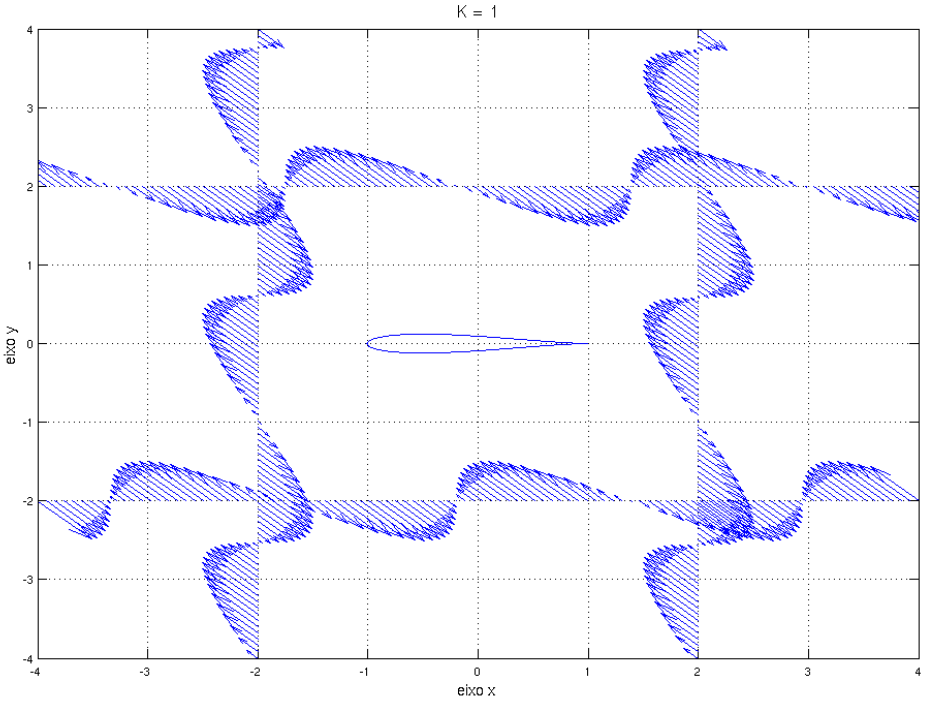

Figure 4.2: Airfoil in a two-dimensional, periodic gust ($k = 1.0$)

Figure 4.3 illustrates the vorticity field imposed by the vortical-gust.

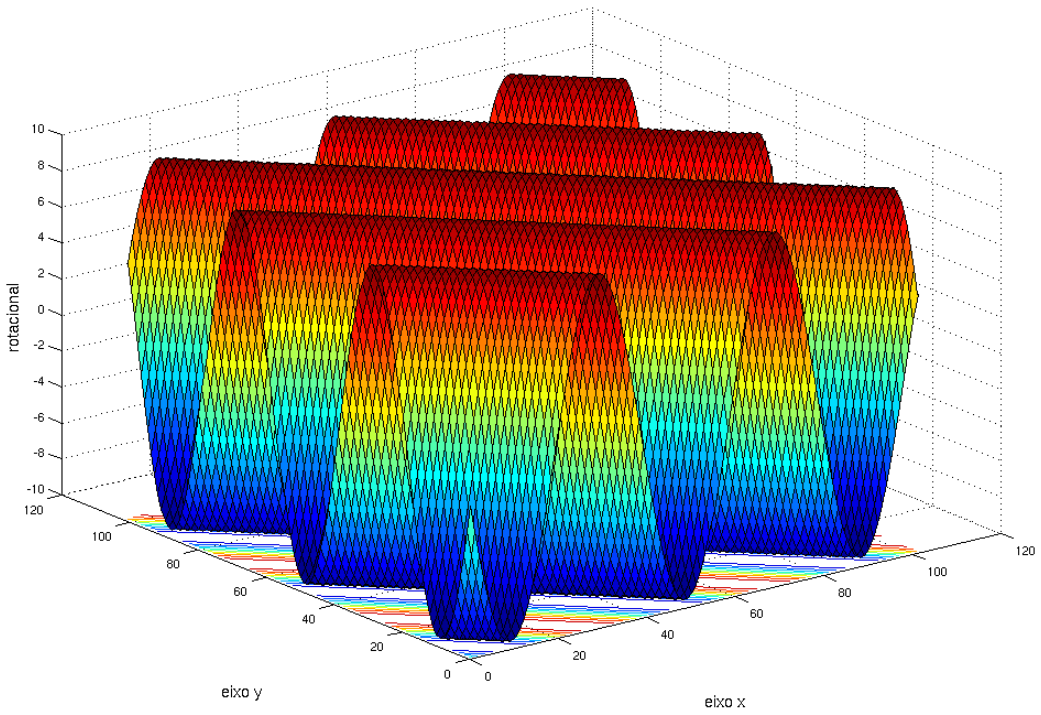

Figure 4.3: vorticity field imposed by the vortical-gust for $k = 1$

In order to establish a time dependent flow field, a time dependent acceleration is imposed as follow.

$$g_x = \frac{\partial U_x}{\partial t} = U_\infty k_x a_x \sin[(x - U_\infty t)k_x + y k_y] \tag{4.4}$$

$$g_y = \frac{\partial U_y}{\partial t} = U_\infty k_x a_y \sin[(x - U_\infty t)k_x + y k_y] \tag{4.5}$$

where g_x and g_y are the x and y components of the acceleration imposed on the field.

4.2 Geometry: the joukowski airfoils

The problem will be solved for a Joukowski airfoil that can be genereted as follows. Set

$$\zeta_1 = r_0 e^{i\theta} + \zeta_0 \tag{4.6}$$

where

$$\zeta_0 = -\epsilon_1 + i\epsilon_2 \tag{4.7}$$

is a complex constant. Letting $z = x - iy$ denote the airfoil coordinates in the complex z plane, the transformation

$$z = (\zeta_1 + \frac{d^2}{\zeta_1} e^{-i\alpha}) \tag{4.8}$$

transform the ζ_1 circle defined by equation 4.6 into the desired airfoil shape.

For Case 1, use $r_0 = 0.54632753$, $\epsilon_1 = 0.05062004$, $\epsilon_2 = 0$, $d^2 = 0.24572591$, $\alpha = 0$ and $0 < \theta < 2\pi$. Figure 4.4 illustrates the airfoil for Case 1.

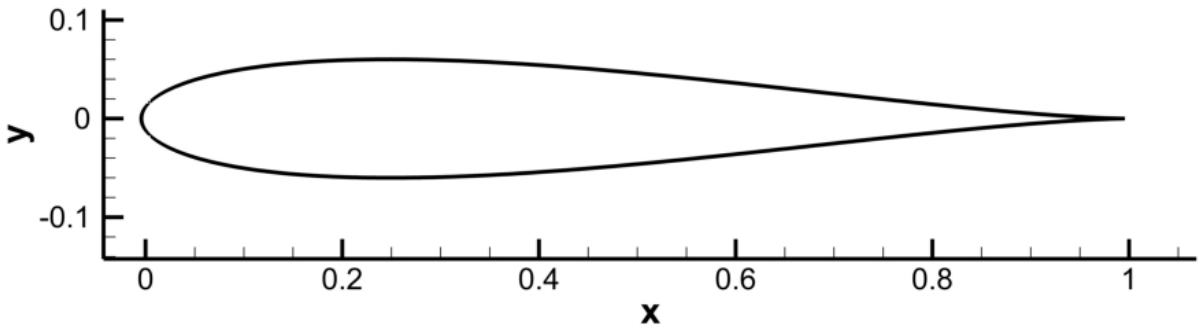

Figure 4.4: Airfoil geometry for Case 1

For Case 2, use $r_0 = 0.54676443$, $\epsilon_1 = 0.05062004$, $\epsilon_2 = 0.02185310$, $d^2 = 0.24572591$, $\alpha = 0.034906585$ and $-\beta < \theta < 2\pi - \beta$ where $\beta = 0.039978687$. Figure 4.5 illustrates the airfoil for Case 2.

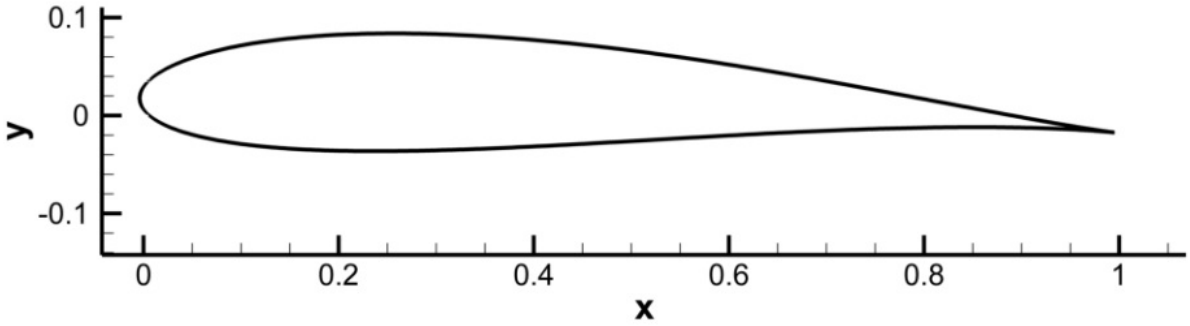

Figure 4.5: Airfoil geometry for Case 2

The above procedure generate a Joukowski airfoil of chord length 2, situated very nearly between $x = -1$ and $x = 1$. To generate the geometry a MatLab 7 routine was created.

4.3 Geometry details

The virtual Aeroacoustic Tunnel (VAT) uses the immersed boundary method, wich uses two distinct meshes; the eulerian mesh, a cartesian regular mesh, wich represents the control volumes located all over the flow field and the lagrangean mesh, wich indicates the points that determinates the geometry immersed in the flow. Since it is necessary to fill all the volumes of the eulerian mesh with points of the lagrangean mesh indicating the normal direction of the surface, the trailing edge was modified to meet immersed boundary mesh requirements. Figure 4.6 and 4.7shows the trucaded trailing edge.

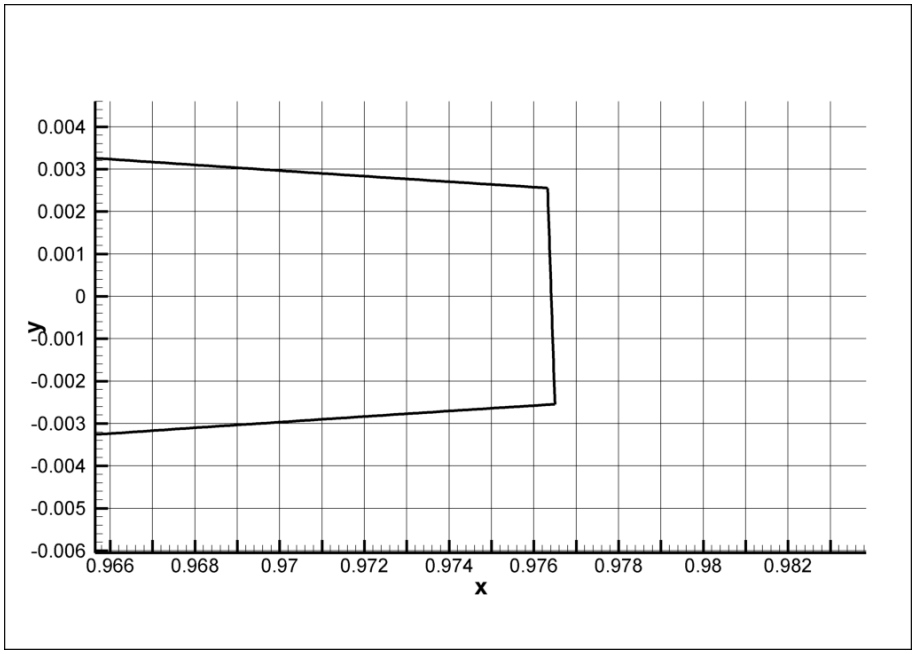

Figure 4.6: Truncaded Trailing edge of Case 1 airfoil

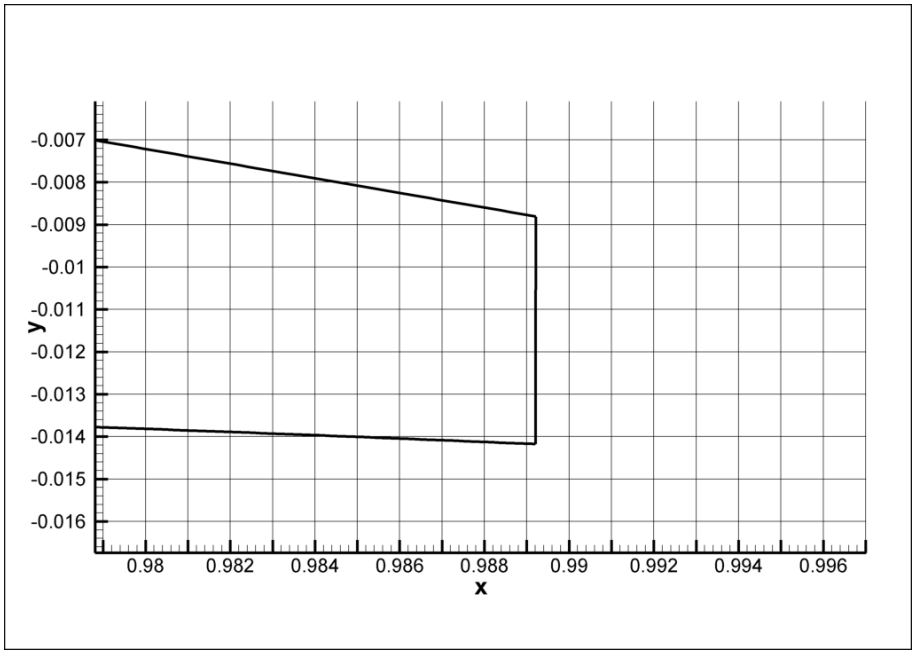

Figure 4.7: Truncaded Trailing edge of Case 2 airfoil

5 GOVERNING EQUATIONS

For study purposes the Continuum Hypothesis is assumed. Thus, it starts from the fundament that a fluid particle can be defined and it is big enough when compared to the molecular scales and small enough when compared to the proposed problem dimensions. Therefore, being the fluid continuous, the obtained equations for a control volume are also continuous and differential. The present work is based on mass, momentum and energy conservation equations in their differential and nondimensional formulation, beyond others constitutive equations which are detailed below.

Every variable is non-dimensionalized according to Anderson *et al* (1983), proposal. Thereunto, characteristic variables such as the freestream flow velocity, U^*_∞, and the problem characteristic lenght, L^*, are used. It is important to note that '$*$' indicates dimensional variables and '∞' indicates freestream properties.

$$
\begin{gathered}
x = \frac{x^*}{L^*}, \quad y = \frac{y^*}{L^*}, \quad z = \frac{z^*}{L^*}, \quad t = \frac{t^*}{L^*/U^*_\infty}, \\
u = \frac{u^*}{U^*_\infty}, \quad v = \frac{v^*}{U^*_\infty}, \quad w = \frac{w^*}{U^*_\infty}, \\
p = \frac{p^*}{\rho^*_\infty \left(U^*_\infty\right)^2}, \quad \rho = \frac{\rho^*}{\rho^*_\infty}, \\
T = \frac{T^*}{T^*_\infty}, \quad e = \frac{e^*}{\left(U^*_\infty\right)^2}, \quad \mu = \frac{\mu^*}{\mu^*_\infty}, \quad f = \frac{f^*}{\rho^*_\infty \left(U^*_\infty\right)^2 / L^*}.
\end{gathered} \tag{5.1}
$$

Where, x, y and z are the spatial coordinates, u, v e w are the velocity vector components in the **i**, **j** and **k** directions, t is the temporal coordinate, ρ is the fluid density, p is the thermodynamic pressure, T is the temperature, e is the internal energy per unit mass and μ is dynamic viscosity.

The continuity equation or mass conservation equation is:

$$
\frac{\partial \rho}{\partial t} + \frac{\partial}{\partial x_i}\left(\rho u_i\right) = 0, \tag{5.2}
$$

The above equation shows that mass is conserved throughout the control volume, whereas mass can not be created nor destroyed. Since Eq. (5.2) is in conservative formulation, the first term represents the temporal variation of mass inside the control volume and the second term represents the mass flux through the control volume i.e.the advective term.

The momentum equation is given by:

$$
\frac{\partial}{\partial t}\left(\rho u_i\right) + \frac{\partial}{\partial x_j}\left(\rho u_i u_j\right) = -\frac{\partial p}{\partial x_i} + \frac{\partial \tau_{ij}}{\partial x_j} + f_i, \tag{5.3}
$$

Where, p is the thermodynamic pressure and τ_{ij} is the shear stress tensor. On the left side, the first term represents the mass temporal variation and the second term represents the momentum net flux through the control volume. On the right side, the first term represents the pressure field force and the second term represents the shear stress forces.

The shear stress tensor, τ_{ij}, is given by Eq. (5.4) below. The first term is the straining rate.

$$\tau_{ij} = \frac{1}{\mathrm{Re}}\left(\mu S_{ij}\right) = \frac{1}{\mathrm{Re}}\left\{\mu\left[\left(\frac{\partial u_i}{\partial x_j} + \frac{\partial u_j}{\partial x_i}\right) - \frac{2}{3}\delta_{ij}\frac{\partial u_k}{\partial x_k}\right]\right\}, \tag{5.4}$$

Where μ is the dynamic viscosity, δ_{ij} is the Kronecker's delta and Re is the Reynolds number, defined as:

$$\mathrm{Re} = \frac{\rho^*_\infty U^*_\infty L^*}{\mu^*_\infty}. \tag{5.5}$$

Finally, the energy equation is:

$$\frac{\partial}{\partial t}\left(\rho e_T\right) + \frac{\partial}{\partial x_i}\left(\rho e_T u_i\right) = -\frac{\partial}{\partial x_i}\left(p u_i\right) + \frac{\partial}{\partial x_i}\left(\tau_{ij} u_j\right) - \frac{\partial q_i}{\partial x_i} + f_i u_i. \tag{5.6}$$

In the above equation it is known that ρe_T is the total energy per unit volume. Thus, on the left side the first term represents the temporal variation of total energy and the second represents the flux of total energy through the control surface in i-direction. On the right side, the first term refers to the work due to the pressure field force and the second terms represents the work due to shear stresses. The third term is the heat transferred and q_i represents the heat flux density in i-direction.

The Fourier equation, provides the q_i components according to Eq. (5.7):

$$q_i = -\mathrm{k}\left(\frac{\partial T}{\partial x_i}\right), \tag{5.7}$$

Or in the non-dimensionalized form, Eq (5.8):

$$q_i = -\frac{\mu}{\left(\gamma - 1\right)\, M^2\, \mathrm{Re}\, \mathrm{Pr}}\left(\frac{\partial T}{\partial x_i}\right). \tag{5.8}$$

Where k is the thermal conductivity, γ is the specific heat ratio under constant pressure and volume and M and Pr are Mach and Prandtl numbers as follows:

$$M = \frac{U^*_\infty}{\sqrt{\gamma\, R^*\, T^*_\infty}}, \qquad \mathrm{Pr} = \frac{c^*_p}{k^*_\infty}\mu^*_\infty. \tag{5.9}$$

The physical meaning of the Prandtl number is the ratio between momentum diffusivity and thermal diffusivity, while Mach number represents the ratio between the flow velocity and the sound velocity.

The total energy per unit mass is the sum of internal energy (e) and kinetic energy (e_k):

$$e_T = e + e_k = c_v T + \frac{u_i\, u_i}{2} \tag{5.10}$$

The above equations total five scalar equations, but contain seven variables: u, p, ρ, e, T, μ and k. Hence, four constitutive equations are needed.

Treating air as a thermally and calorically perfect gas, i.e. c_v is constant:

$$e = c_v T \tag{5.11}$$

For the compressible flow of a perfect gas, the relation between pressure and temperature as showed by Anderson (1990) is:

$$p = (\gamma - 1)\, \rho e \tag{5.12}$$

$$T = \frac{\gamma\, M^2\, p}{\rho}. \tag{5.13}$$

Anderson (1990) evidences that dynamic viscosity is given by Sutherland equation:

$$\mu = C_1 \frac{T^{3/2}}{T + C_2}, \quad C_1 = \left[\frac{\left(T_\infty^*\right)^{1/2}}{\mu_\infty^*}\right] C_1^*, \quad C_2 = \frac{C_2^*}{T_\infty^*}, \tag{5.14}$$

Where C_1^* and C_2^* are dimensional constants.

For a calorically perfect gas, thermal conductivity k is:

$$k = \mu \frac{c_p}{Pr}. \tag{5.15}$$

In order to avoid the numerical oscillations resulting from the discrete forcing approach used by the immersed boundary methodology, a volume pseudo-force (f_i) and its associated volume pseudo-work ($f_i u_i$) are introduced in the right-hand side of the momentum and energy equations in order to continuously accelerate, using a non-inertial frame of reference, the entire flow field from the stagnation condition to the free-flow condition during the acceleration time, t_a. For a free-flow velocity aligned with the Cartesian x-direction ($\mathbf{u}_\infty = U_\infty^* \mathbf{i}$) the only component of the pseudo-force f_i is

$$f_x = \frac{f_x^*}{\rho_\infty^* \left(U_\infty^*\right)^2 / L^*} = \frac{\rho^* \left(U_\infty^* / t_a^*\right)}{\rho_\infty^* \left(U_\infty^*\right)^2 / L^*} = \left(\frac{\rho^*}{\rho_\infty^*}\right) \left(\frac{L^* / U_\infty^*}{t_a^*}\right) = \frac{\rho}{t_a}, \tag{5.16}$$

for $t \leq t_a$. After this acceleration time, the value of the pseudo-force f_i must be zero, since the free-flow conditions are achieved, resulting in

$$f_x = 0, \tag{5.17}$$

for $t > t_a$.

To impose the acceleration necessary to establish the vortical gust a pseudo-force (g_i) and its associated volume pseudo-work ($g_i u_i$) are introduced in the right-hand side on the momentum and energy equations. The x and y component of this pseudo-force are given by

$$g_x = -k\rho\epsilon\frac{\sqrt{2}}{2}\sin[k(x+y-t)] \tag{5.18}$$

$$g_y = +k\rho\epsilon\frac{\sqrt{2}}{2}\sin[k(x+y-t)] \tag{5.19}$$

The present work is interested in the instabilities genereted by the advective therm of the momentum equation. In this focus a compressible and inviscid abordation is more interesting. The fisical meaning of Euler equations take into account that the Reynolds number tends to infinity. So $\tau_{ij} = 0$ tends to zero.

Taking $\tau_{ij} = 0$, the Unsteady nonlinear Euler equations are given by:

$$\frac{\partial \rho}{\partial t} + \frac{\partial}{\partial x_i}(\rho u_i) = 0, \tag{5.20}$$

$$\frac{\partial}{\partial t}(\rho u_i) + \frac{\partial}{\partial x_j}(\rho u_i u_j) = -\frac{\partial p}{\partial x_i} + f_i, \tag{5.21}$$

$$\frac{\partial}{\partial t}(\rho e_T) + \frac{\partial}{\partial x_i}(\rho e_T u_i) = -\frac{\partial}{\partial x_i}(p u_i) - \frac{\partial q_i}{\partial x_i} + f_i u_i + . \tag{5.22}$$

Since the gust amplitude $\vec{a}$ satisfies $|\vec{a}| \ll U_\infty$, the linearized Unstedy Euler equations can be solved.

$$\frac{\partial}{\partial t}(\rho_0 + \rho') + \frac{\partial}{\partial x_i}[(\rho u_i)_0] + (\rho u_i)'] = 0, \tag{5.23}$$

$$\frac{\partial}{\partial t}\left[(\rho u_i)_0 + (\rho u_i)'\right] + \frac{\partial}{\partial x_j}\left[(\rho u_i)_0 u_{j0} + (\rho u_i)' u_{j0} + (\rho u_i)_0 u'_j + \right] = -\frac{\partial}{\partial x_i}(p_0 + p') + f_i + g_i, \tag{5.24}$$

$$\frac{\partial}{\partial t}\left[(\rho e_T)_0 + (\rho e_T)'\right] + \frac{\partial}{\partial x_i}\left[(\rho e_T)_0 u_{i0} + (\rho e_T)' u_{i0} + (\rho e_T)_0 u'_i\right] = -\frac{\partial}{\partial x_i}(p_0 u_{i0} + p_0 u'_i + p' u_{i0}) + f_i(u_{i0} + u'_i) + g_i(u_{i0} + u'_i) \tag{5.25}$$

The nondimensional upstream velocity is given by:

$$U_x = -\epsilon\frac{\sqrt{2}}{2}\cos[k(x+y-t)] \tag{5.26}$$

$$U_y = +\epsilon\frac{\sqrt{2}}{2}\cos[k(x+y-t)] \tag{5.27}$$

The nondimensional acceleration imposed on the field to induce the upstream velocity described above is

$$\frac{\partial U_x}{\partial t} = -k\epsilon\frac{\sqrt{2}}{2}\sin[k(x+y-t)] \tag{5.28}$$

$$\frac{\partial U_x}{\partial t} = +k\epsilon\frac{\sqrt{2}}{2}\sin[k(x+y-t)] \tag{5.29}$$

5.1 Numerical Method

In order to numerically solve the unsteady compressible Euler equations using a finite volume approach, Eqs. (5.20), (5.21) and (5.22) are written in the vector form

$$\frac{\partial \mathbf{U}}{\partial t} + \frac{\partial \mathbf{E}}{\partial x} + \frac{\partial \mathbf{F}}{\partial y} + \frac{\partial \mathbf{G}}{\partial z} = \mathbf{R}, \tag{5.30}$$

where the vectors **U**, **E**, **F**, **G** and **R** are given by

$$\mathbf{U} = \begin{bmatrix} \rho \\ \rho u \\ \rho v \\ \rho w \\ \rho e_T \end{bmatrix}, \tag{5.31}$$

$$\mathbf{E} = \begin{bmatrix} \rho u \\ \rho u^2 + p \\ \rho uv \\ \rho uw \\ (\rho e_T + p)\, u \end{bmatrix}, \tag{5.32}$$

$$\mathbf{F} = \begin{bmatrix} \rho v \\ \rho vu \\ \rho v^2 + p \\ \rho vw \\ (\rho e_T + p)\, v \end{bmatrix} \tag{5.33}$$

$$\mathbf{G} = \begin{bmatrix} \rho w \\ \rho wu \\ \rho wv \\ \rho w^2 + p \\ (\rho e_T + p)\, w \end{bmatrix}, \tag{5.34}$$

$$\mathbf{R} = \begin{bmatrix} 0 \\ f_x + g_x + g_y \\ 0 \\ 0 \\ (f_x + g_x + g_y)u \end{bmatrix}. \tag{5.35}$$

For the linearized Euler equations, the vectors $\mathbf{U}$, $\mathbf{E}$, $\mathbf{F}$, $\mathbf{G}$ and $\mathbf{R}$ are given by

$$\mathbf{U} = \begin{bmatrix} \rho_0 + \rho' \\ (\rho u)_0 + (\rho u)' \\ (\rho v)_0 + (\rho v)' \\ (\rho w)_0 + (\rho w)' \\ (\rho e_T)_0 + (\rho e_T)' \end{bmatrix}, \tag{5.36}$$

$$\mathbf{E} = \begin{bmatrix} (\rho u)_0 + (\rho u)' \\ (\rho u)_0 u_0 + (\rho u)_0 u' + (\rho u)' u_0 + p_0 + p' \\ (\rho u)_0 v_0 + (\rho u)_0 v' + (\rho u)' v_0 \\ (\rho u)_0 w_0 + (\rho u)_0 w' + (\rho u)' w_0 \\ \left[(\rho e_T)_0 + p_0\right] u_0 + \left[(\rho e_T)' + p'\right] u_0 + \left[(\rho e_T)_0 + p_0\right] u' \end{bmatrix}, \tag{5.37}$$

$$\mathbf{F} = \begin{bmatrix} (\rho v)_0 + (\rho v)' \\ (\rho v)_0 u_0 + (\rho v)_0 u' + (\rho v)' u_0 \\ (\rho v)_0 v_0 + (\rho v)_0 v' + (\rho v)' v_0 + p_0 + p' \\ (\rho v)_0 w_0 + (\rho v)_0 w' + (\rho v)' w_0 \\ \left[(\rho e_T)_0 + p_0\right] v_0 + \left[(\rho e_T)' + p'\right] v_0 + \left[(\rho e_T)_0 + p_0\right] v' \end{bmatrix}, \tag{5.38}$$

$$\mathbf{G} = \begin{bmatrix} (\rho w)_0 + (\rho w)' \\ (\rho w)_0 u_0 + (\rho w)_0 u' + (\rho w)' u_0 \\ (\rho w)_0 v_0 + (\rho w)_0 v' + (\rho w)' v_0 \\ (\rho w)_0 w_0 + (\rho w)_0 w' + (\rho w)' w_0 + p_0 + p' \\ \left[(\rho e_T)_0 + p_0\right] w_0 + \left[(\rho e_T)' + p'\right] w_0 + \left[(\rho e_T)_0 + p_0\right] w' \end{bmatrix}, \tag{5.39}$$

$$\mathbf{R} = \begin{bmatrix} 0 \\ f_x + g_x + g_y \\ 0 \\ 0 \\ (f_x + g_x + g_y) u_0 + (f_x + g_x + g_y) u' \end{bmatrix}. \tag{5.40}$$

Defining tensor Π as

$$\Pi = \mathbf{E} \otimes \mathbf{i} + \mathbf{F} \otimes \mathbf{j} + \mathbf{G} \otimes \mathbf{k}, \tag{5.41}$$

Eq. (5.30) is rewritten as

$$\frac{\partial \mathbf{U}}{\partial t} + \nabla \cdot \Pi = \mathbf{R}. \tag{5.42}$$

Integrating the above equation over the control volume V, and applying the divergence theorem to the first term of the right-hand side results

$$\frac{\partial}{\partial t} \int_V \mathbf{U} dV = - \int_V (\nabla \cdot \Pi)\, dV + \int_V \mathbf{R} dV = - \int_S (\Pi \cdot \mathbf{n})\, dS + \int_V \mathbf{R} dV, \tag{5.43}$$

Defining the volumetric mean of vectors $\overline{\mathbf{U}}$ and $\overline{\mathbf{R}}$ in the control volume V as

$$\overline{\mathbf{U}} \equiv \frac{1}{V}\int_V \mathbf{U} dV \tag{5.44}$$

and

$$\overline{\mathbf{R}} \equiv \frac{1}{V}\int_V \mathbf{R} dV, \tag{5.45}$$

respectively, Eq. (5.43) is written as

$$\frac{\partial \overline{\mathbf{U}}}{\partial t} = -\frac{1}{V}\int_S (\Pi \cdot \mathbf{n}) dS + \overline{\mathbf{R}}. \tag{5.46}$$

For the volume (i, j, k), the first-order approximation of the temporal derivative is given by

$$\left(\frac{\partial \overline{\mathbf{U}}}{\partial t}\right)_{i,j,k} = \frac{\Delta \overline{\mathbf{U}}_{i,j,k}}{\Delta t} + O\left(\Delta t\right), \tag{5.47}$$

and the temporal approximation of Eq. (5.47) for a hexahedral control volume is

$$\begin{aligned} \Delta \overline{\mathbf{U}}_{i,j,k} \;=\; & -\frac{\Delta t}{V_{i,j,k}}\left[\int_{S_{i+1/2}} (\Pi \cdot \mathbf{n})\, dS + \int_{S_{i-1/2}} (\Pi \cdot \mathbf{n})\, dS + \right. \\ & \int_{S_{j+1/2}} (\Pi \cdot \mathbf{n})\, dS + \int_{S_{j-1/2}} (\Pi \cdot \mathbf{n})\, dS + \\ & \left. \int_{S_{k+1/2}} (\Pi \cdot \mathbf{n})\, dS + \int_{S_{k-1/2}} (\Pi \cdot \mathbf{n})\, dS \right] + \Delta t \overline{\mathbf{R}}, \end{aligned} \tag{5.48}$$

where $S_{i+1/2}, S_{i-1/2}, S_{j+1/2}, S_{j-1/2}, S_{k+1/2}$ e $S_{k-1/2}$ are the surfaces that define the hexahedral control volume and $S_{i+1/2}$ is the common surface between volume (i, j, k) and volume $(i + 1, j, k)$.

Considering that the value of tensor Π is constant over the control surfaces, it is possible to define $\mathcal{F}(\overline{\mathbf{U}})_{i,j,k}$ as a function of the flux of tensor Π over the control surfaces as

$$\begin{aligned} \mathcal{F}(\overline{\mathbf{U}})_{i,j,k} \;=\; & -\frac{\Delta t}{V_{i,j,k}}\left[(\Pi \cdot \mathbf{S})_{i+1/2} + (\Pi \cdot \mathbf{S})_{i-1/2} + \right. \\ & (\Pi \cdot \mathbf{S})_{j+1/2} + (\Pi \cdot \mathbf{S})_{j-1/2} + \\ & \left. (\Pi \cdot \mathbf{S})_{k+1/2} + (\Pi \cdot \mathbf{S})_{k-1/2}\right] + \Delta t \overline{\mathbf{R}}, \end{aligned} \tag{5.49}$$

and the resulting spatial approximation of Eq. (5.48) is

$$\Delta \overline{\mathbf{U}}_{i,j,k} = \mathcal{F}\left(\overline{\mathbf{U}}\right)_{i,j,k} + \mathcal{D}\left(\overline{\mathbf{U}}\right)_{i,j,k} \tag{5.50}$$

where $\mathcal{D}(\overline{\mathbf{U}})_{i,j,k}$ is an explicit artificial dissipation. In order to calculate $\mathcal{F}(\overline{\mathbf{U}})_{i,j,k}$, the flux of tensor Π over the control surfaces must be calculated. For the control surface

$S_{i+1/2}$, this flux is given by

$$(\Pi \cdot \mathbf{S})_{i+1/2} = \begin{bmatrix} (\Pi \cdot \mathbf{S})_1 \\ (\Pi \cdot \mathbf{S})_2 \\ (\Pi \cdot \mathbf{S})_3 \\ (\Pi \cdot \mathbf{S})_4 \\ (\Pi \cdot \mathbf{S})_5 \end{bmatrix}_{i+1/2} . \tag{5.51}$$

The first component of the vector defined by the above equation is associated to the continuity equation and given by

$$(\Pi \cdot \mathbf{S})_1 = \rho_{i+1/2} \, (q_s)_{i+1/2} \, , \tag{5.52}$$

where the volumetric flux is

$$(q_s)_{i+1/2} = \mathbf{u}_{i+1/2} \cdot \mathbf{S}_{i+1/2} = u_{i+1/2} \, (s_x)_{i+1/2} + v_{i+1/2} \, (s_y)_{i+1/2} + w_{i+1/2} \, (s_z)_{i+1/2} \, . \tag{5.53}$$

The second, third, and fourth components are associated to the three components of the momentum equation and are respectively given by

$$(\Pi \cdot \mathbf{S})_2 = \, (\rho u)_{i+1/2} \, (q_s)_{i+1/2} + p_{i+1/2} \, (s_x)_{i+1/2} \, , \tag{5.54}$$

$$(\Pi \cdot \mathbf{S})_3 = \, (\rho v)_{i+1/2} \, (q_s)_{i+1/2} + p_{i+1/2} \, (s_y)_{i+1/2} \, , \tag{5.55}$$

and,

$$(\Pi \cdot \mathbf{S})_4 = \, (\rho w)_{i+1/2} \, (q_s)_{i+1/2} + p_{i+1/2} \, (s_z)_{i+1/2} \, . \tag{5.56}$$

The fifth component is associated with the energy equation and given by

$$(\Pi \cdot \mathbf{S})_5 = \, (\rho e_T)_{i+1/2} \, (q_s)_{i+1/2} + p_{i+1/2} \, (q_s)_{i+1/2} \, . \tag{5.57}$$

For the linearized Euler equations, the first component of the vector defined by the above equation is associated to the continuity equation and given by

$$(\Pi \cdot \mathbf{S})_1 = (\rho_0)_{i+1/2} \left[(q_s)_0 \right]_{i+1/2} + (\rho_0)_{i+1/2} \left[(q_s)' \right]_{i+1/2} + (\rho')_{i+1/2} \left[(q_s)_0 \right]_{i+1/2} , \tag{5.58}$$

where the volumetric flux of the time-averaged and perturbation velocities are given by

$$\left[(q_s)_0 \right]_{i+1/2} = (u_0)_{i+1/2} \, (s_x)_{i+1/2} + (v_0)_{i+1/2} \, (s_y)_{i+1/2} + (w_0)_{i+1/2} \, (s_z)_{i+1/2} \, , \tag{5.59}$$

and

$$\left[(q_s)' \right]_{i+1/2} = (u')_{i+1/2} \, (s_x)_{i+1/2} + (v')_{i+1/2} \, (s_y)_{i+1/2} + (w')_{i+1/2} \, (s_z)_{i+1/2} \, , \tag{5.60}$$

respectevely. The second, third, and fourth components are associated to the three components of the momentum equation and are respectively given by

$$\begin{aligned}(\Pi\cdot\mathbf{S})_2 &= [(\rho u)_0]_{i+1/2}\,[(q_s)_0]_{i+1/2} + (p_0)_{i+1/2}\,(s_x)_{i+1/2} + \left[(\rho u)'\right]_{i+1/2}[(q_s)_0]_{i+1/2} + \\ &\quad [(\rho u)_0]_{i+1/2}\left[(q_s)'\right]_{i+1/2} + (p')_{i+1/2}\,(s_x)_{i+1/2} \end{aligned} \tag{5.61}$$

$$\begin{aligned}(\Pi\cdot\mathbf{S})_3 &= [(\rho v)_0]_{i+1/2}\,[(q_s)_0]_{i+1/2} + (p_0)_{i+1/2}\,(s_x)_{i+1/2} + \left[(\rho v)'\right]_{i+1/2}[(q_s)_0]_{i+1/2} + \\ &\quad [(\rho v)_0]_{i+1/2}\left[(q_s)'\right]_{i+1/2} + (p')_{i+1/2}\,(s_x)_{i+1/2} \end{aligned} \tag{5.62}$$

and,

$$\begin{aligned}(\Pi\cdot\mathbf{S})_4 &= [(\rho w)_0]_{i+1/2}\,[(q_s)_0]_{i+1/2} + (p_0)_{i+1/2}\,(s_x)_{i+1/2} + \left[(\rho w)'\right]_{i+1/2}[(q_s)_0]_{i+1/2} + \\ &\quad [(\rho w)_0]_{i+1/2}\left[(q_s)'\right]_{i+1/2} + (p')_{i+1/2}\,(s_x)_{i+1/2} \end{aligned} \tag{5.63}$$

The fifth component is associated with the energy equation and given by

$$\begin{aligned}(\Pi\cdot\mathbf{S})_5 &= \left\{[(\rho e_T)_0]_{i+1/2} + (p_0)_{i+1/2}\right\}[(q_s)_0]_{i+1/2} + \left\{[(\rho e_T)_0]_{i+1/2} + (p_0)_{i+1/2}\right\}\left[(q_s)'\right]_{i+1/2} \\ &\quad \left\{\left[(\rho e_T)'\right]_{i+1/2} + (p')_{i+1/2}\right\}[(q_s)_0]_{i+1/2} \end{aligned} \tag{5.64}$$

In order to calculate the flux $(\Pi\cdot\mathbf{S})$ according to Eqs. (5.52) to (5.57), it is necessary to approximate the values of the variables at the control surface $\mathbf{S}_{i+1/2}$ from the mean values of the conservative variables in the control volumes, given by the vectors

$$\overline{\mathbf{U}}_{i,j,k} = \begin{bmatrix} \overline{\rho} \\ \overline{\rho u} \\ \overline{\rho v} \\ \overline{\rho w} \\ \overline{\rho e_T} \end{bmatrix}_{i,j,k} = \begin{bmatrix} \overline{\rho}_0 + \overline{\rho}' \\ (\overline{\rho u})_0 + (\overline{\rho u})' \\ (\overline{\rho v})_0 + (\overline{\rho v})' \\ (\overline{\rho w})_0 + (\overline{\rho w})' \\ (\overline{\rho e_T})_0 + (\overline{\rho e_T})' \end{bmatrix}_{i,j,k} \tag{5.65}$$

In order to obtain the momentum and energy primitive variables, the Favre mean is used to calculate the mass-averaged momentum and energy primitive variables as

$$\widetilde{u} = \frac{\overline{\rho u}}{\overline{\rho}}, \quad \widetilde{v} = \frac{\overline{\rho v}}{\overline{\rho}}, \quad \widetilde{w} = \frac{\overline{\rho w}}{\overline{\rho}}, \quad \widetilde{e_T} = \frac{\overline{\rho e_T}}{\overline{\rho}}. \tag{5.66}$$

$$\widetilde{u}_0 = \frac{(\overline{\rho u})_0}{\overline{\rho}_0}, \quad \widetilde{v}_0 = \frac{(\overline{\rho v})_0}{\overline{\rho}_0}, \quad \widetilde{w}_0 = \frac{(\overline{\rho w})_0}{\overline{\rho}_0}, \quad \widetilde{e_{T0}} = \frac{(\overline{\rho e_T})_0}{\overline{\rho}_0}. \tag{5.67}$$

$$\widetilde{u}' = \frac{(\overline{\rho u})'}{\overline{\rho}'}, \quad \widetilde{v}' = \frac{(\overline{\rho v})'}{\overline{\rho}'}, \quad \widetilde{w}' = \frac{(\overline{\rho w})'}{\overline{\rho}'}, \quad \widetilde{e_T}' = \frac{(\overline{\rho e_T})'}{\overline{\rho}'}. \tag{5.68}$$

The mean of the total energy is given by

$$\widetilde{e}_T = \widetilde{e} + \widetilde{e}_k = \widetilde{e} + \frac{\widetilde{uu} + \widetilde{vv} + \widetilde{ww}}{2}. \tag{5.69}$$

$$(\widetilde{e}_T)_0 = \widetilde{e}_0 + (\widetilde{e}_k)_0 = \widetilde{e}_0 + \frac{(\widetilde{uu})_0 + (\widetilde{vv})_0 + (\widetilde{ww})_0}{2}. \tag{5.70}$$

$$(\widetilde{e}_T)' = \widetilde{e}' + (\widetilde{e}_k)' = \widetilde{e}' + \frac{(\widetilde{uu})' + (\widetilde{vv})' + (\widetilde{ww})'}{2}. \tag{5.71}$$

Since it is not possible to directly calculate the mass-averaged kinetic energy, given by the second term of the right-hand side of the above equation, the internal energy is calculated as

$$\underline{e} = \widetilde{e}_T - \underline{e}_k = \widetilde{e}_T - \frac{\widetilde{u}\widetilde{u} + \widetilde{v}\widetilde{v} + \widetilde{w}\widetilde{w}}{2}, \tag{5.72}$$

$$\underline{e}_0 = (\widetilde{e}_T)_0 - (\underline{e}_k)_0 = (\widetilde{e}_T)_0 - \frac{\widetilde{u}_0\widetilde{u}_0 + \widetilde{v}_0\widetilde{v}_0 + \widetilde{w}_0\widetilde{w}_0}{2}, \tag{5.73}$$

$$\underline{e}' = (\widetilde{e}_T)' - (\underline{e}_k)' = (\widetilde{e}_T)' - \frac{\widetilde{u}'\widetilde{u}' + \widetilde{v}'\widetilde{v}' + \widetilde{w}'\widetilde{w}'}{2}, \tag{5.74}$$

and the mean of the thermodynamic variables p and T are calculated as

$$\underline{p} = (\gamma - 1)\,\overline{\rho}\;\underline{e}, \quad \underline{T} = \frac{\gamma\, M^2\, \underline{p}}{\overline{\rho}}, \tag{5.75}$$

$$\underline{p}_0 = (\gamma - 1)\,\overline{\rho}_0\;\underline{e}_0, \quad \underline{T}_0 = \frac{\gamma\, M^2\, \underline{p}_0}{\overline{\rho}_0}, \tag{5.76}$$

$$\underline{p}' = (\gamma - 1)\,\overline{\rho}'\;\underline{e}', \quad \underline{T}' = \frac{\gamma\, M^2\, \underline{p}'}{\overline{\rho}'}. \tag{5.77}$$

It is important to note that the first terms in the right-hand side of Eqs. (5.52), (5.54), (5.55), (5.56), and (5.57) are the fluxes of mass, momentum and total energy through surface $\mathbf{S}_{i+1/2}$ and the other terms are fluxes that are functions of the right-hand sides of the momentum and total energy equations. In order to evaluate all this terms at that surface, in this work is used the fourth-order skew-symmetric scheme proposed by Ducros Ducros *et al* (2000), et al. where

$$u_{i+1/2} = \frac{2}{3}\left(\widetilde{u}_i + \widetilde{u}_{i+1}\right) - \frac{1}{12}\left(\widetilde{u}_{i-1} + \widetilde{u}_i + \widetilde{u}_{i+1} + \widetilde{u}_{i+2}\right), \tag{5.78}$$

$$(u_0)_{i+1/2} = \frac{2}{3}\left[(\widetilde{u}_0)_i + (\widetilde{u}_0)_{i+1}\right] - \frac{1}{12}\left[(\widetilde{u}_0)_{i-1} + (\widetilde{u}_0)_i + (\widetilde{u}_0)_{i+1} + (\widetilde{u}_0)_{i+2}\right], \tag{5.79}$$

$$(u')_{i+1/2} = \frac{2}{3}\left[(\widetilde{u}')_i + (\widetilde{u}')_{i+1}\right] - \frac{1}{12}\left[(\widetilde{u}')_{i-1} + (\widetilde{u}')_i + (\widetilde{u}')_{i+1} + (\widetilde{u}')_{i+2}\right], \tag{5.80}$$

for the primitive variables, exemplified in the above equation by the $x-$direction component of the velocity, and where

$$(\rho u)_{i+1/2} = \frac{2}{3}\left[(\overline{\rho u})_i + (\overline{\rho u})_{i+1}\right] - \frac{1}{12}\left[(\overline{\rho u})_{i-1} + (\overline{\rho u})_i + (\overline{\rho u})_{i+1} + (\overline{\rho u})_{i+2}\right], \tag{5.81}$$

$$[(\rho u)_0]_{i+1/2} = \frac{2}{3}\{[(\overline{\rho u})_0]_i + [(\overline{\rho u})_0]_{i+1}\} - \frac{1}{12}\{[(\overline{\rho u})_0]_{i-1} + [(\overline{\rho u})_0]_i + [(\overline{\rho u})_0]_{i+1} + [(\overline{\rho u})_0]_{i+2}\}, \tag{5.82}$$

$$\left[(\rho u)'\right]_{i+1/2} = \frac{2}{3}\{\left[(\overline{\rho u})'\right]_i + \left[(\overline{\rho u})'\right]_{i+1}\} - \frac{1}{12}\{\left[(\overline{\rho u})'\right]_{i-1} + \left[(\overline{\rho u})'\right]_i + \left[(\overline{\rho u})'\right]_{i+1} + \left[(\overline{\rho u})'\right]_{i+2}\}, \tag{5.83}$$

for the conservative variables, also exemplified by the $x-$direction component of the specific momentum.

The scheme proposed by Eqs. (5.78) to (5.83) is a centered one, and therefore, an explicit artificial viscosity was previously included in Eq. (5.50). In order to enhance the numerical method with shock-capturing capabilities and the ability to cope with steep gradient regions, this artificial dissipation uses the basic idea proposed by Jameson *et al* (1981), given by

$$\mathcal{D}(\overline{\mathbf{U}}) = [d_{i+1/2}(\overline{\mathbf{U}}) - d_{i-1/2}(\overline{\mathbf{U}})] + [d_{j+1/2}(\overline{\mathbf{U}}) - d_{j-1/2}(\overline{\mathbf{U}})] + [d_{k+1/2}(\overline{\mathbf{U}}) - d_{k-1/2}(\overline{\mathbf{U}})], \tag{5.84}$$

where

$$d_{i+1/2}(\overline{\mathbf{U}}) = \epsilon^{(2)}_{i+1/2}[\overline{\mathbf{U}}_{i+1} - \overline{\mathbf{U}}_i] - \epsilon^{(4)}_{i+1/2}[\overline{\mathbf{U}}_{i+2} - 3\overline{\mathbf{U}}_{i+1} + 3\overline{\mathbf{U}}_i - \overline{\mathbf{U}}_{i-1}]. \tag{5.85}$$

The first and second terms of Eq. (5.85) are second-order and fourth-order dissipation operators, respectively. The first one acts in the shock and the second one acts over steep gradient regions, like the viscous regions. The coefficients of Eq. (5.85) are given by

$$\epsilon^{(2)}_{i+1/2} = K^{(2)}\max\left(\Psi_i, \Psi_{i+1}\right), \qquad \epsilon^{(4)}_{i+1/2} = \max\left[0, \left(K^{(4)} - \epsilon^{(2)}_{i+1/2}\right)\right], \tag{5.86}$$

where

$$K^{(2)} = 1/4, \qquad K^{(4)} = 1/256, \tag{5.87}$$

and sensor Ψ_i is given by

$$\Psi_i = \frac{|\underline{p}_{i+1} - 2\underline{p}_i + \underline{p}_{i-1}|}{|\underline{p}_{i+1}| + |2\underline{p}_i| + |\underline{p}_{i-1}|}. \tag{5.88}$$

This dissipation model was successfully applied in the numerical simulation of vortex-shock interactions in laminar flows Bobenrieth (2005), unsteady aerodynamic forces over circular cylinders in transonic flow Bobenrieth *et al.* (2006a), , the effect of plunging and pitching motions over an airfoil in transonic laminar flow Bobenrieth *et al.* (2006b), , the effect of the plunging velocity over an airfoil in subsonic laminar flow Bobenrieth (2006c), and subsonic, transonic, and supersonic cavity flows Bobenrieth (2008). It was also recently applied in the direct computation of noise generated by stator cascades Bobenrieth *et al.* (2010), .

The proposed vorticity-based sensor,

$$(\Psi_{\text{rot}})_{i+1/2} = K^{(2)}_{\text{rot}} \cdot |\nabla \times \mathbf{u}|_{i+1/2}, \tag{5.89}$$

and the proposed divergence-based sensor,

$$(\Psi_{\text{div}})_{i+1/2} = K^{(2)}_{\text{div}} \cdot |\nabla \cdot \mathbf{u}|_{i+1/2}, \tag{5.90}$$

are implemented in the artificial dissipation model by substituting the pressure-based sensor in the calculation of the coefficient of the second-order dissipation operator as

$$\epsilon^{(2)}_{i+1/2} = \max\left[(\Psi_{\text{rot}})_{i+1/2}, (\Psi_{\text{div}})_{i+1/2}\right]. \tag{5.91}$$

Since the calculation of the divergence and the vorticity of the velocity field is fourth-order acurate in space, the resulting numerical method is fourth-order accurate in space and third-order accurate in time.

In order to advance Eq. (5.50) in time, a third-order Runge-Kutta is used as proposed by Shu and reported by Yee (1997). This yield to the following three steps:

$$\overline{\mathbf{U}}^1 = \overline{\mathbf{U}}^n - \left[\mathcal{F}\left(\overline{\mathbf{U}}^n\right) - \mathcal{D}\left(\overline{\mathbf{U}}^n\right)\right], \tag{5.92}$$

$$\overline{\mathbf{U}}^2 = \frac{3}{4}\overline{\mathbf{U}}^n + \frac{1}{4}\overline{\mathbf{U}}^1 - \frac{1}{4}\left[\mathcal{F}\left(\overline{\mathbf{U}}^1\right) - \mathcal{D}\left(\overline{\mathbf{U}}^1\right)\right], \tag{5.93}$$

$$\overline{\mathbf{U}}^{n+1} = \frac{1}{3}\overline{\mathbf{U}}^n + \frac{2}{3}\overline{\mathbf{U}}^2 - \frac{2}{3}\left[\mathcal{F}\left(\overline{\mathbf{U}}^2\right) - \mathcal{D}\left(\overline{\mathbf{U}}^2\right)\right]. \tag{5.94}$$

As used in this work, the resulting numerical method is fourth-order accurate in space and third-order accurate in time. The immersed boundary methodology is applied in the manner described by Bobenrieth *et al.*(2009), .

5.2 Immersed-Boundary Technique

The approach used in this work for imposing the boundary conditions at the boundary volumes, defined as the control volumes that contain one or more surface-grid points, is a discrete forcing one where the boundary conditions are directly imposed directly to the boundary volumes. In all the control volumes, the mean values of the conservative variables are given by

$$\overline{\mathbf{U}}_{i,j,k} = \begin{bmatrix} \overline{\rho} \\ \overline{\rho}\widetilde{u} \\ \overline{\rho}\widetilde{v} \\ \overline{\rho}\widetilde{w} \\ \overline{\rho}\,\widetilde{e_T} \end{bmatrix}_{i,j,k}. \tag{5.95}$$

In the boundary volumes, the no-slip condition directly results in the boundary values

$$\widetilde{u} = \widetilde{v} = \widetilde{w} = 0. \tag{5.96}$$

Since the total energy is the sum of the internal and kinetic energy, the application of the no-slip condition in Eq. (5.72) results in

$$\widetilde{e_T} = \underline{e}, \tag{5.97}$$

bearing, for the boundary volumes

$$\overline{\mathbf{U}}^{\,b}_{i,j,k} = \begin{bmatrix} \overline{\rho} \\ 0 \\ 0 \\ 0 \\ \underline{e} \end{bmatrix}^{b}_{i,j,k}, \tag{5.98}$$

where the superscript b indicates that the finite volume (i, j, k) is a boundary volume. It is important to note that the number of boundary volumes is less or equal to the number of surface points, since more than one surface points can lie within one boundary volume.

In order to obtain the boundary values for the density, $\overline{\rho}$, and the internal energy, $\underline{e}$, the averaged equation of state,

$$\underline{p} = \left(\frac{1}{\gamma M_\infty^2}\right) \overline{\rho}\, \underline{T}, \tag{5.99}$$

is derived in the normal outward direction from the solid wall. With this objective, it is defined $\mathbf{n}$ as a unit vector with a direction that is normal to the wall with outward sense, where the Cartesian components are $\mathbf{n} = n_x\mathbf{i} + n_y\mathbf{j} + n_z\mathbf{k}$ and the magnitude is $|\mathbf{n}| = \sqrt{n_x^2 + n_y^2 + n_y^2} = 1$. Depending on the resolution of the Cartesian and surface grids, more than one surface point can lie within a boundary volume, and in this case it is used the mean among all normal unit vectors associated to the grid points that lie within the boundary volume. With the normal direction defined by one unit vector in the boundary volume or by an averaged unit vector over the boundary volume, the derivative in this direction is given by

$$\frac{\partial \underline{p}}{\partial n} = \left(\frac{1}{\gamma M_\infty^2}\right) \frac{\partial}{\partial n} \left(\overline{\rho}\, \underline{T}\right) = \left(\frac{1}{\gamma M_\infty^2}\right) \left(\overline{\rho} \frac{\partial \underline{T}}{\partial n} + \underline{T} \frac{\partial \overline{\rho}}{\partial n}\right). \tag{5.100}$$

For an adiabatic wall, $\partial \underline{T}/\partial n = 0$, and considering the boundary-layer approximation, $\partial \underline{p}/\partial n = 0$, Eq. (5.100) yields

$$\frac{\partial \overline{\rho}}{\partial n} = 0, \tag{5.101}$$

and since

$$\underline{e} = \frac{1}{\gamma(\gamma - 1) M_\infty^2} \underline{T}, \tag{5.102}$$

the adiabatic wall condition results in

$$\frac{\partial \underline{e}}{\partial n} = 0. \tag{5.103}$$

Defining $\mathbf{n}$ as a unit vector with a direction that is normal to the solid wall and a sense that is outward with Cartesian components $\mathbf{n} = n_x\mathbf{i} + n_y\mathbf{j} + n_z\mathbf{k}$, the derivates of the averaged density and internal energy are written as

$$\frac{\partial \overline{\rho}}{\partial n} = \frac{\partial \overline{\rho}}{\partial x}\frac{\partial x}{\partial n} + \frac{\partial \overline{\rho}}{\partial y}\frac{\partial y}{\partial n} + \frac{\partial \overline{\rho}}{\partial z}\frac{\partial z}{\partial n} = n_x\frac{\partial \overline{\rho}}{\partial x} + n_y\frac{\partial \overline{\rho}}{\partial y} + n_z\frac{\partial \overline{\rho}}{\partial z} \tag{5.104}$$

and

$$\frac{\partial \underline{e}}{\partial n} = \frac{\partial \underline{e}}{\partial x}\frac{\partial x}{\partial n} + \frac{\partial \underline{e}}{\partial y}\frac{\partial y}{\partial n} + \frac{\partial \underline{e}}{\partial z}\frac{\partial z}{\partial n} = n_x\frac{\partial \underline{e}}{\partial x} + n_y\frac{\partial \underline{e}}{\partial y} + n_z\frac{\partial \underline{e}}{\partial z}. \tag{5.105}$$

For the boundary volumes, Eqs. (5.101) and (5.103) apply and result in

$$0 = n_x\left(\frac{\partial \overline{\rho}}{\partial x}\right)^b_{i,j,k} + n_y\left(\frac{\partial \overline{\rho}}{\partial y}\right)^b_{i,j,k} + n_z\left(\frac{\partial \overline{\rho}}{\partial z}\right)^b_{i,j,k} \tag{5.106}$$

and

$$0 = n_x\left(\frac{\partial \underline{e}}{\partial x}\right)^b_{i,j,k} + n_y\left(\frac{\partial \underline{e}}{\partial y}\right)^b_{i,j,k} + n_z\left(\frac{\partial \underline{e}}{\partial z}\right)^b_{i,j,k}. \tag{5.107}$$

If $n_x > 0$, in regular region of the Cartesian grid the derivative $\partial\overline{\rho}/\ \partial x$ in the boundary volumes can be calculated with fourth-order spatial precision using a forward finite-difference approach as

$$\left(\frac{\partial \overline{\rho}}{\partial x}\right)^b_{i,j,k} = \frac{1}{12\Delta x}\left[-25\overline{\rho}^b_{i,j,k} + 48\overline{\rho}_{i+1,j,k} - 36\overline{\rho}_{i+2,j,k} + 16\overline{\rho}_{i+3,j,k} - 3\overline{\rho}_{i+4,j,k} + O(\Delta x)^4\right]. \tag{5.108}$$

Defining the difference operator

$$D^+_i\overline{\rho} = \frac{1}{25}\left(48\overline{\rho}_{i+1,j,k} - 36\overline{\rho}_{i+2,j,k} + 16\overline{\rho}_{i+3,j,k} - 3\overline{\rho}_{i+4,j,k}\right), \tag{5.109}$$

Eq. (5.108) is written as

$$\left(\frac{\partial \overline{\rho}}{\partial x}\right)_{i,j,k} = \frac{25}{12\Delta x}\left[-\overline{\rho}^b_{i,j,k} + D^+_i\overline{\rho} + O(\Delta x)^4\right]. \tag{5.110}$$

If $\mathbf{n} = \mathbf{i}$ ($n_x = 1$, $n_y = 0$ and $n_z = 0$), Eq. (5.106) gives

$$0 = \left(\frac{\partial \overline{\rho}}{\partial x}\right)^b_{i,j,k}, \tag{5.111}$$

and introducing this result in Eq. (5.110) yields

$$\overline{\rho}^b_{i,j,k} = D^+_i\overline{\rho} + O(\Delta x)^4. \tag{5.112}$$

Following the same line of reasoning, if $\mathbf{n} = \mathbf{j}$ ($n_x = 0$, $n_y = 1$ and $n_z = 0$),

$$\overline{\rho}^{\,b}_{i,j,k} = D_j^+ \overline{\rho} + O(\Delta y)^4, \tag{5.113}$$

and if $\mathbf{n} = \mathbf{k}$ ($n_x = 0$, $n_y = 0$ and $n_z = 1$),

$$\overline{\rho}^{\,b}_{i,j,k} = D_k^+ \overline{\rho} + O(\Delta z)^4. \tag{5.114}$$

For the generalized case, where $\mathbf{n} = n_x\mathbf{i} + n_y\mathbf{j} + n_z\mathbf{k}$, the averaged density is calculated in the boundary volumes as the weighted value

$$\overline{\rho}^{\,b}_{i,j,k} = \frac{|n_x| D_i\overline{\rho} + |n_y| D_j\overline{\rho} + |n_z| D_k\overline{\rho}}{|n_x| + |n_y| + |n_z|}. \tag{5.115}$$

Following an analogous procedure, since $\partial\overline{\rho}/\partial n = \partial\underline{e}/\partial n = 0$, the averaged internal energy is calculated as the weighted value

$$\underline{e}^{\,b}_{i,j,k} = \frac{|n_x| D_i\underline{e} + |n_y| D_j\underline{e} + |n_z| D_k\underline{e}}{|n_x| + |n_y| + |n_z|}, \tag{5.116}$$

where the difference operators (D_i, D_j and D_k) can be in the forward direction (D_i^+, D_j^+ and D_k^+), if the values of n_x, n_y and n_z are positive, or in the backward direction (D_i^-, D_j^- and D_k^-), if the values of n_x, n_y and n_z are negative. For the case of the averaged density, the operator D_i^+ is given by Eq. (5.109), and the other forward and backward difference operators are given by

$$D_j^+\overline{\rho} = \frac{1}{25}\left(48\overline{\rho}_{i,j+1,k} - 36\overline{\rho}_{i,j+2,k} + 16\overline{\rho}_{i,j+3,k} - 3\overline{\rho}_{i,j+4,k}\right), \tag{5.117}$$

$$D_k^+\overline{\rho} = \frac{1}{25}\left(48\overline{\rho}_{i,j,k+1} - 36\overline{\rho}_{i,j,k+2} + 16\overline{\rho}_{i,j,k+3} - 3\overline{\rho}_{i,j,k+4}\right), \tag{5.118}$$

$$D_i^-\overline{\rho} = \frac{1}{25}\left(48\overline{\rho}_{i-1,j,k} - 36\overline{\rho}_{i-2,j,k} + 16\overline{\rho}_{i-3,j,k} - 3\overline{\rho}_{i-4,j,k}\right), \tag{5.119}$$

$$D_j^-\overline{\rho} = \frac{1}{25}\left(48\overline{\rho}_{i,j-1,k} - 36\overline{\rho}_{i,j-2,k} + 16\overline{\rho}_{i,j-3,k} - 3\overline{\rho}_{i,j-4,k}\right), \tag{5.120}$$

$$D_k^-\overline{\rho} = \frac{1}{25}\left(48\overline{\rho}_{i,j,k-1} - 36\overline{\rho}_{i,j,k-2} + 16\overline{\rho}_{i,j,k-3} - 3\overline{\rho}_{i,j,k-4}\right). \tag{5.121}$$

In this manner, the conservative variables vector for the boundary volumes is given by

$$\overline{\mathbf{U}}^{\,b}_{i,j,k} = \begin{bmatrix} \overline{\rho}^{\,b}_{i,j,k} \\ 0 \\ 0 \\ 0 \\ \underline{e}^{\,b}_{i,j,k} \end{bmatrix}, \tag{5.122}$$

where the first and last components are given by Eqs. (5.115) and (5.116), respectively.

6 NUMERICAL SIMULATIONS

6.1 Vat-parameters

In order to solve the Linearized Unsteady Euler Equations a Time-Avagered Flow solution of the Euler equation is necessary. Indeed, analysis of the instantaneus field is necessary to make sure the simulation was carried out in the right way. Since the problems are highly nonlinear ($Re \rightarrow \infty$) numerical errors may occur. This errors are associated with numeric oscilations and a fine adjustment of VAT parameters is necessary to control these oscilations.

6.1.1 Time-step

Time step is an important variable in numeric simulations because it is the time discretization. Since the equations that are solved on VAT have a hyperbolic nature, the Courant-Friedrichs-Lewy condition must be achieved for the numerical solution convergence, Hirsch (2007). VAT uses an explicit time-marching scheme, so it is necessary to control the Courant or CFL number. The CFL is an adimensional number defined as:

$$CFL = \frac{a \triangle t}{\triangle x} \tag{6.1}$$

where a is the convection velocity ($a = U_\infty + c$), $\triangle t$ is the time-step and $\triangle x = L/n_{unit}$, where n_{unit} is the number of elements over the main length.

Ducros *et al* (2000), say that, for this numerical scheme, the local CFL must be $CFL < \sqrt{2}$ on every point of the domain to garantee numerical stability.

For this problem the stream vortices are a low pressure zone. The local velocity and the termodynamic properties are very different from the free stream. So CFL must be a reduced number to garantee numerical stability. Figure 6.1 shows an instantaneus field of a simulation carried out with $CFL = 0.774$ ($time - step = 1.5 * 10^{-6}$) and figure 6.2 shows an instantaneus field for $CFL = 0.516$ ($time - step = 1.0 * 10^{-6}$). Note that for $CFL = 0.516$ the results are satisfactory. Both of the fields showed are for 10^4 iterations, the airfoil is for case 1 (symmetric airfoil).

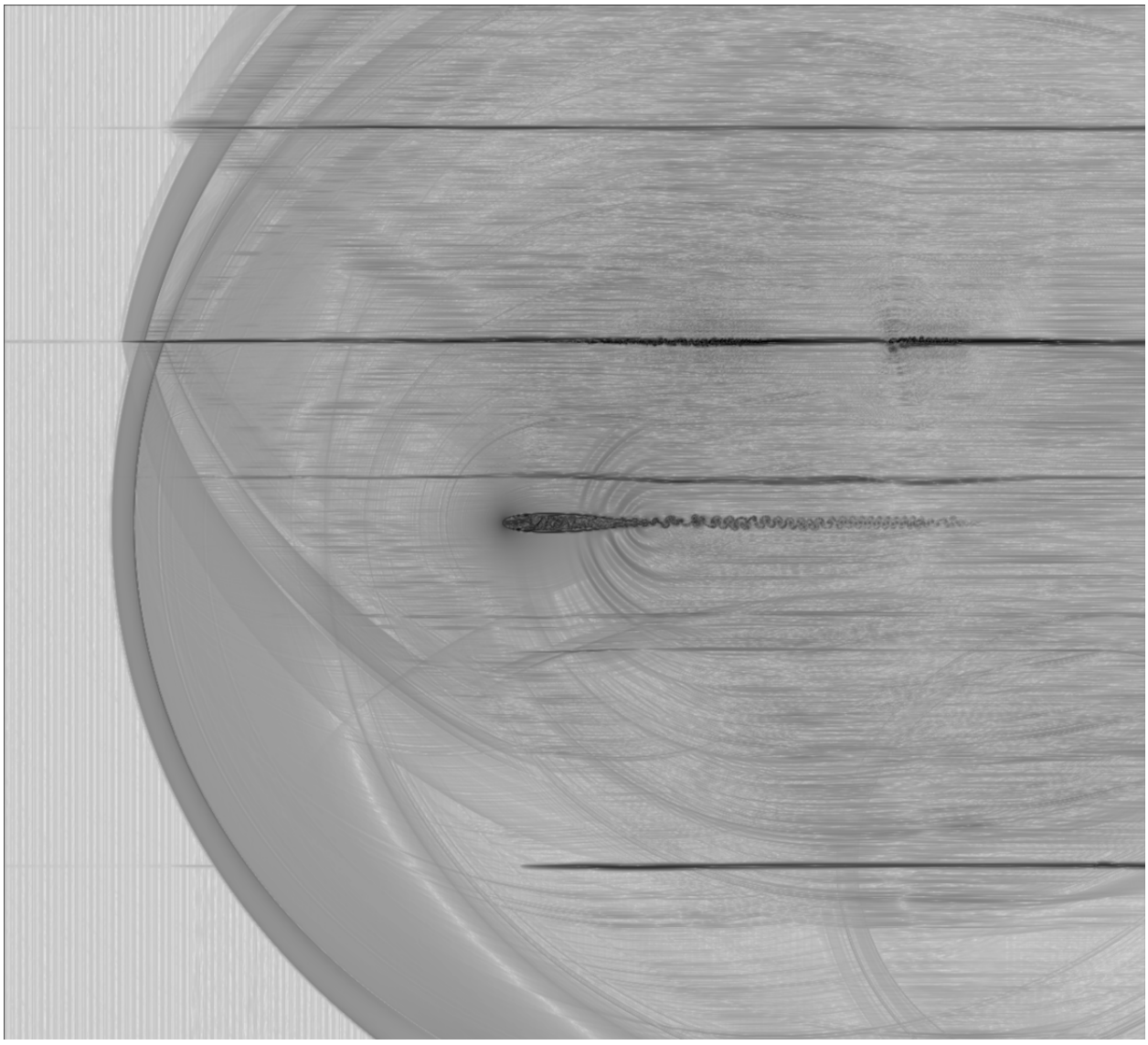

Figure 6.1: numeric oscilations due to nonlinearity of eulers equation. The variable plotted is $\beta_T = |\nabla T|^{1/20}$.

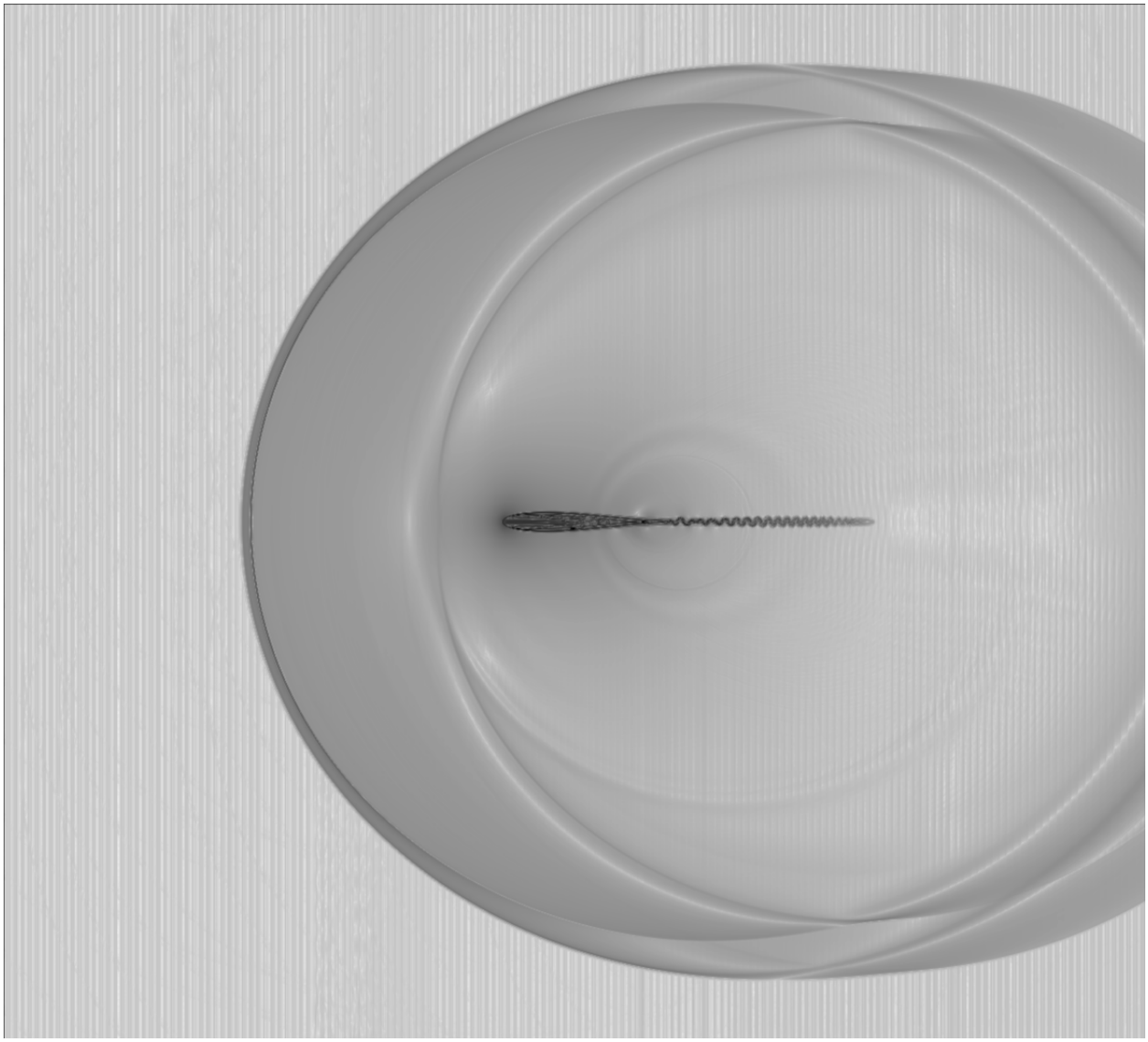

Figure 6.2: instantaneus field of 10^4 iterations for case1. The variable plotted is $\beta_T = |\nabla T|^{1/20}$.

6.1.2 Artificial Viscosity with Pressure Based Sensor

In order to enhance the numerical method with shock-capturing capabilities and the ability to cope with steep gradient regions, VAT uses an artificial dissipation proposed by Jameson *et al* (1981), . This dissipation must control the numeric error without interefe in the fisical meaning of the simulation. Figure 6.3 and 6.4 shows numeric oscilations due to inadequate values of $K^{(2)}$ and $K^{(4)}$, the constants that control the artificial dissipation. Figure 6.5 shows an instantaneus field simulated with the adequate values of $K^{(2)}$ and $K^{(4)}$.

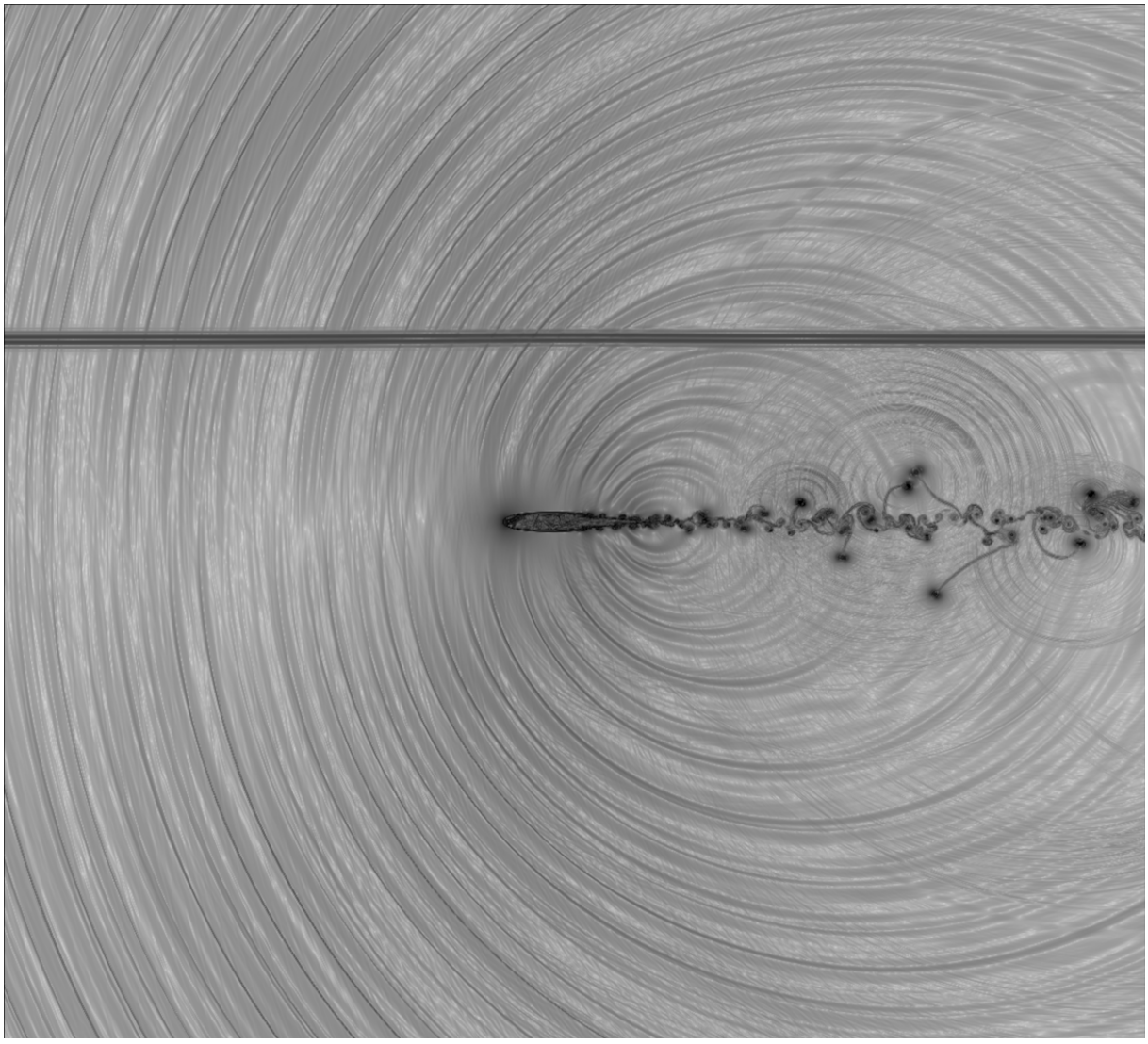

Figure 6.3: instantaneus field of $62 * 10^4$ iterations for case1, $K^{(2)} = 0.25$ and $K^{(4)} = 1/128$. The variable plotted is $\beta_T = |\nabla T|^{1/20}$.

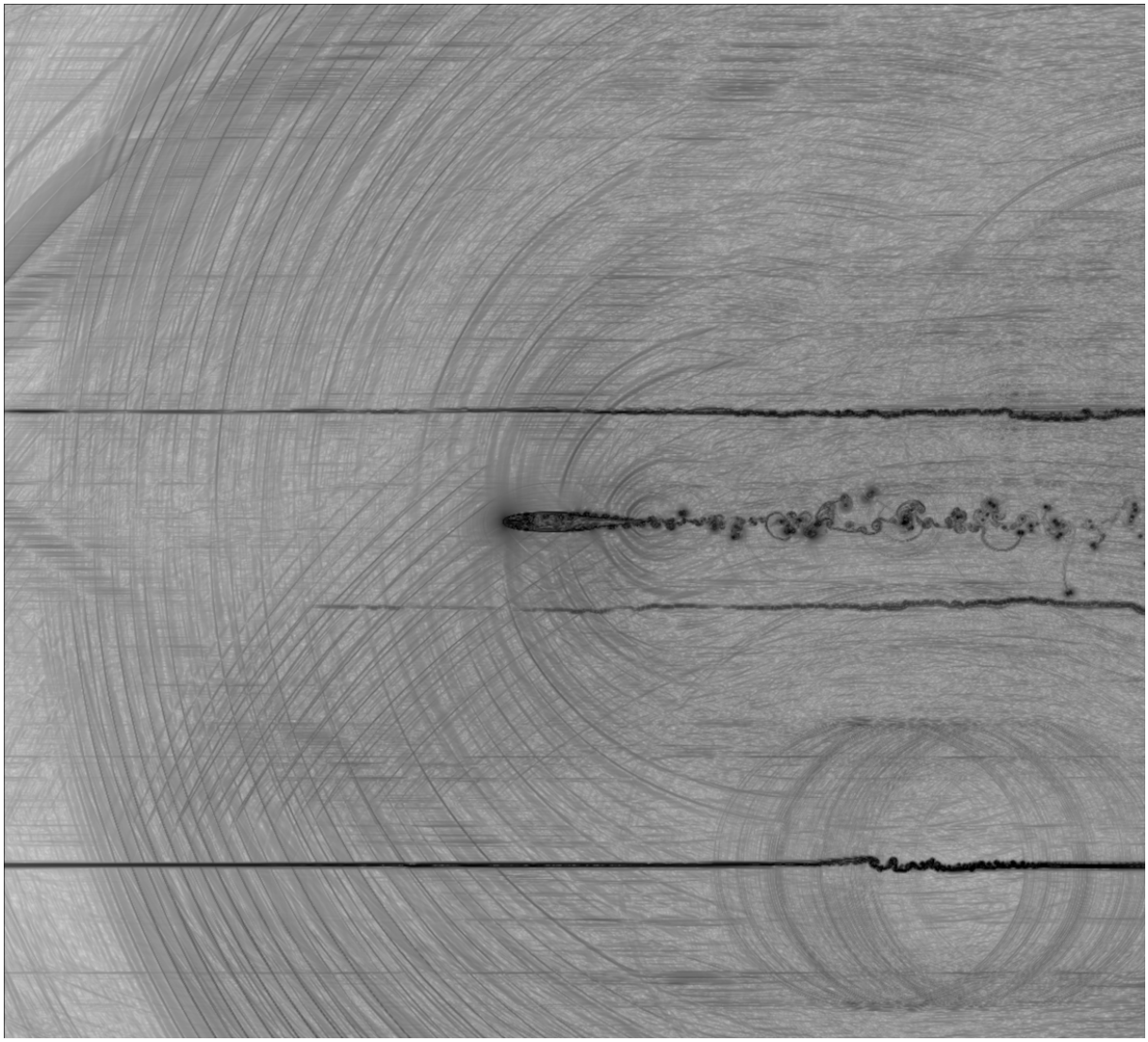

Figure 6.4: instantaneus field of $2 * 10^4$ iterations for case1, $K^{(2)} = 0.175$ and $K^{(4)} = 1/128$. The variable plotted is $\beta_T = |\nabla T|^{1/20}$.

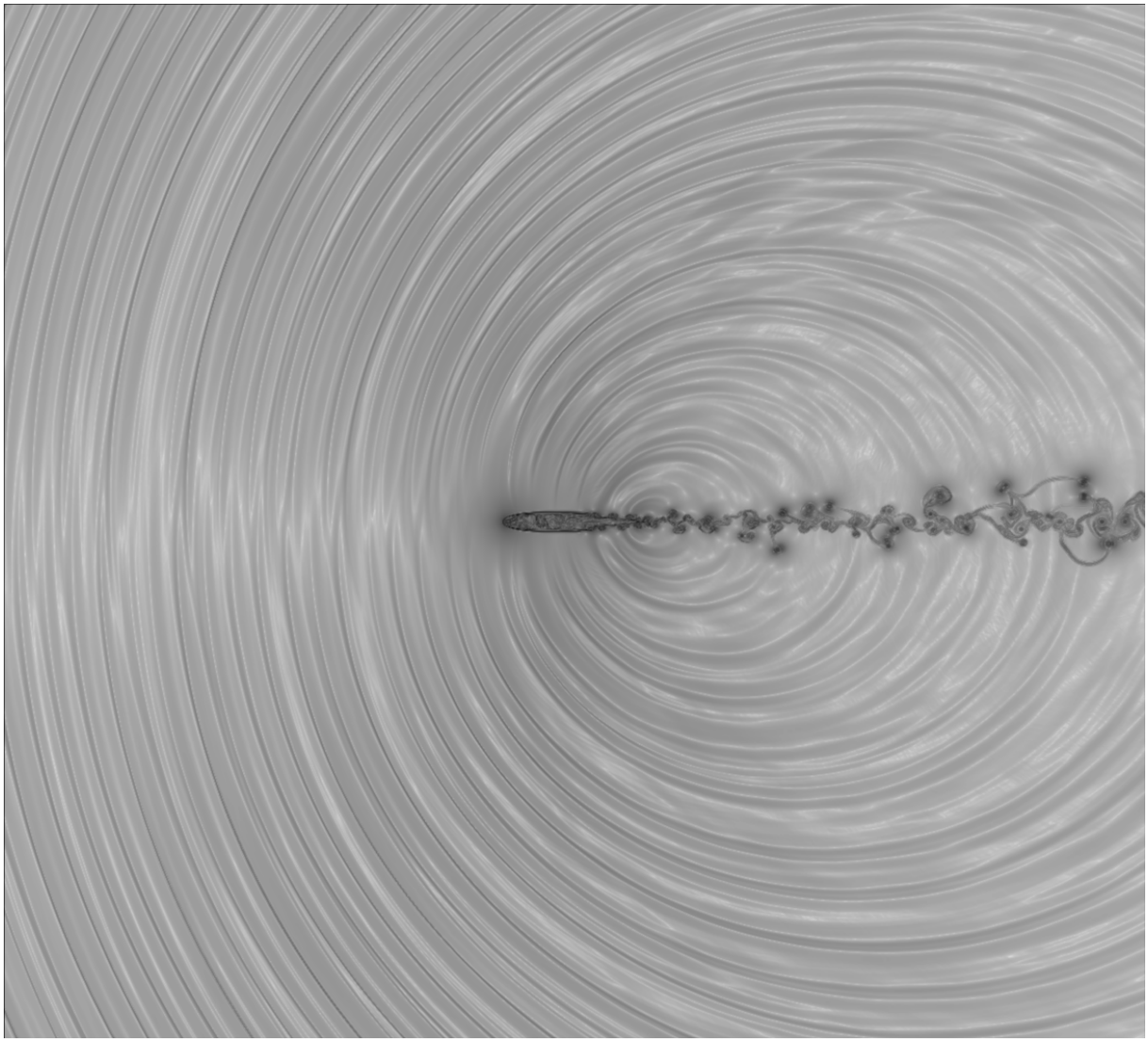

Figure 6.5: instantaneus field of $47 * 10^4$ iterations for case1, $K^{(2)} = 0.5$ and $K^{(4)} = 1/64$. The variable plotted is $\beta_T = |\nabla T|^{1/20}$.

6.2 Time-Averaged Flow Solution with Pressure Based Sensor

In this section preliminary results are shown. The first results are the Euler solutions, since a time-avegered flow solution of the euler equations is necessary to solve the linearized euler equations. All the simulations are two-dimensional, Mach number is 0.5 and one hundred elements along the airfoil chord, a 8x8 chords domain of regular cartesian mesh and a stretch zone of 150 elements in a rate of 1.05 in the directions +x, -x, +y and -y.

Figures 6.6 and 6.7 show acceptable simulations to acquire the time-avered solutions. Figures 6.8 to 6.11 shows intantaneus and mean pressure probes located 4 chords above the airfoil. The probes signal indicates a stablished mean field satisfatory to input data on the linearized-euler simulations.

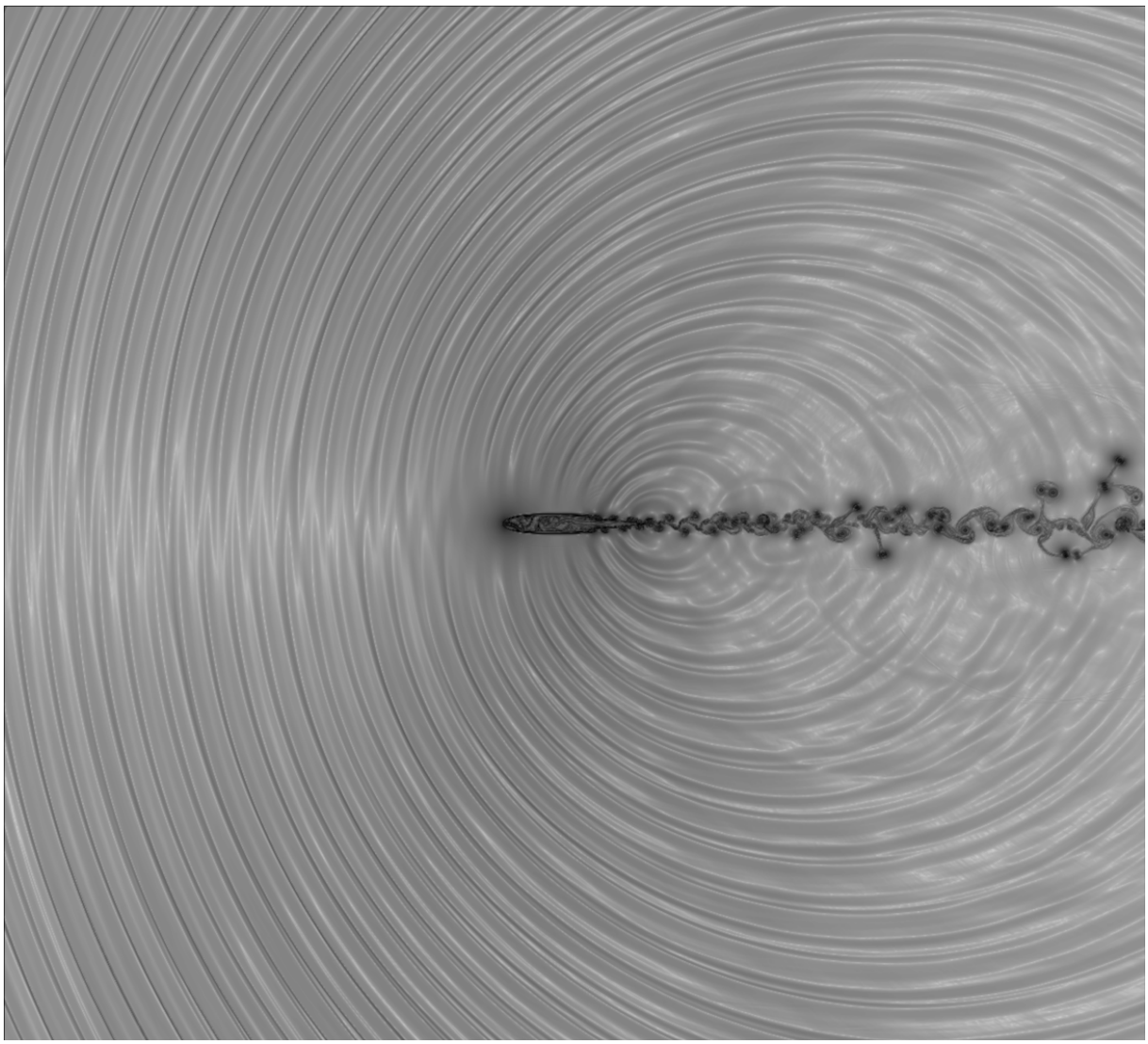

Figure 6.6: Unsteady flow solution for the nonlinear Euler equations for case1. The variable plotted is $\beta_T = |\nabla T|^{1/20}$.

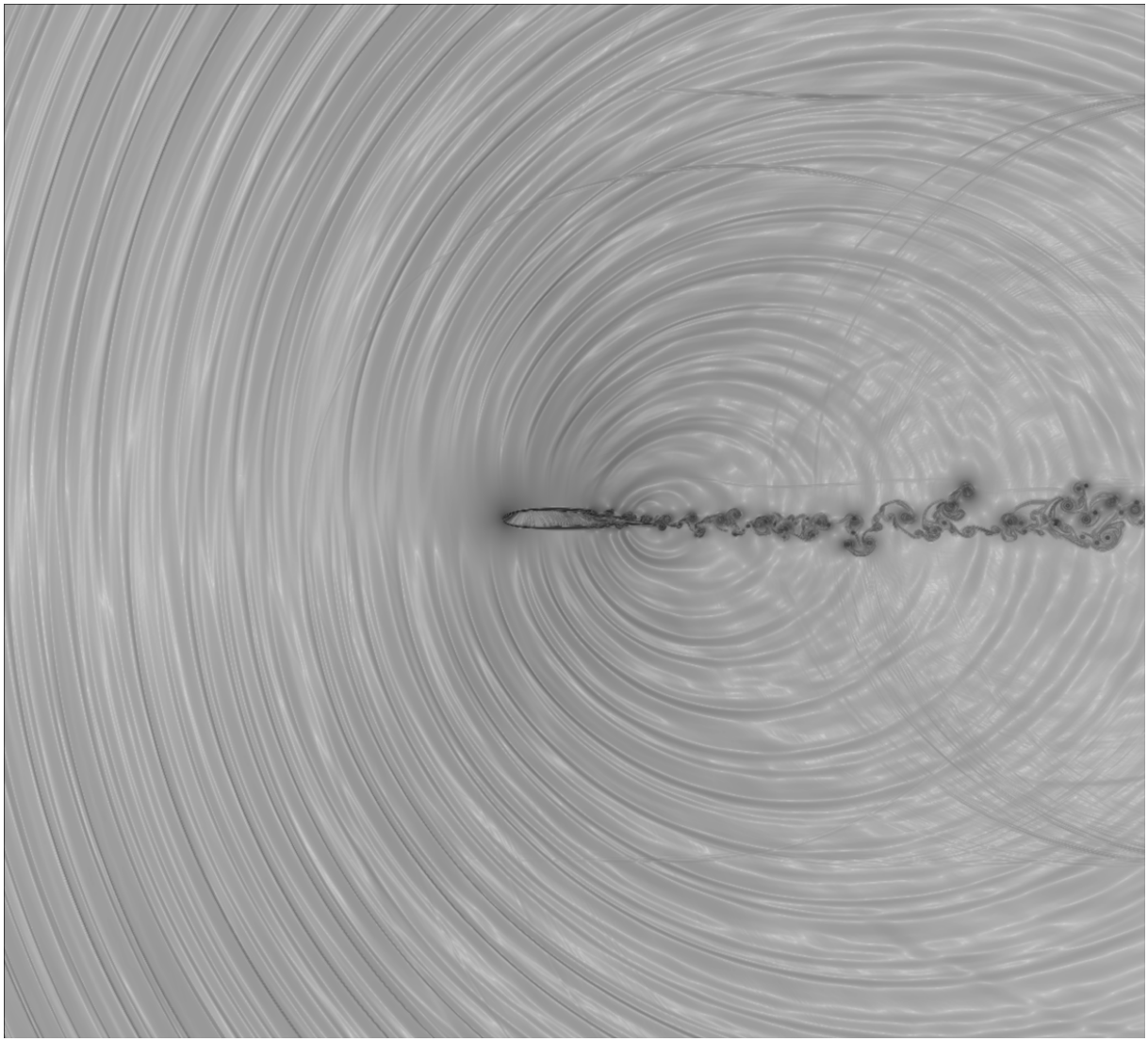

Figure 6.7: Unsteady flow solution for the nonlinear Euler equations for case2. The variable plotted is $\beta_T = |\nabla T|^{1/20}$.

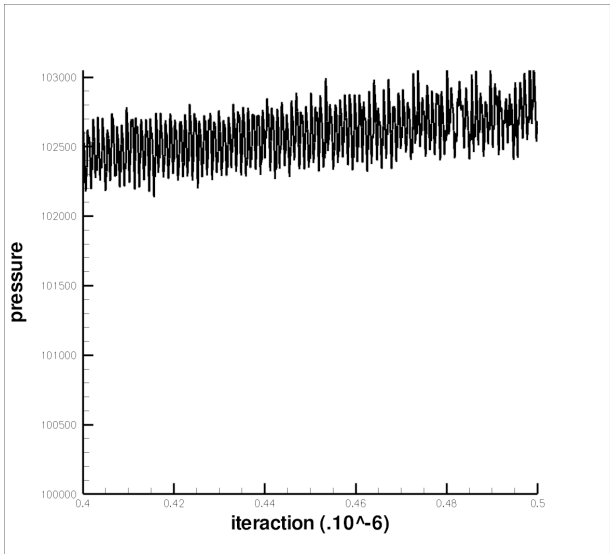

Figure 6.8: pressure probe above the airfoil for case1.

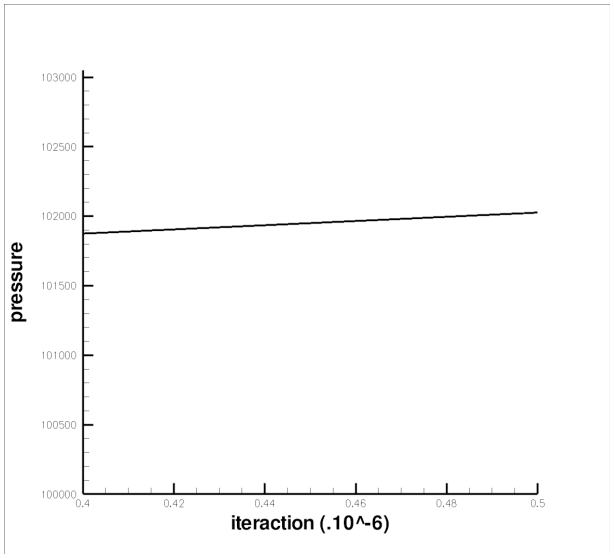

Figure 6.9: mean pressure probe above the airfoil for case1.

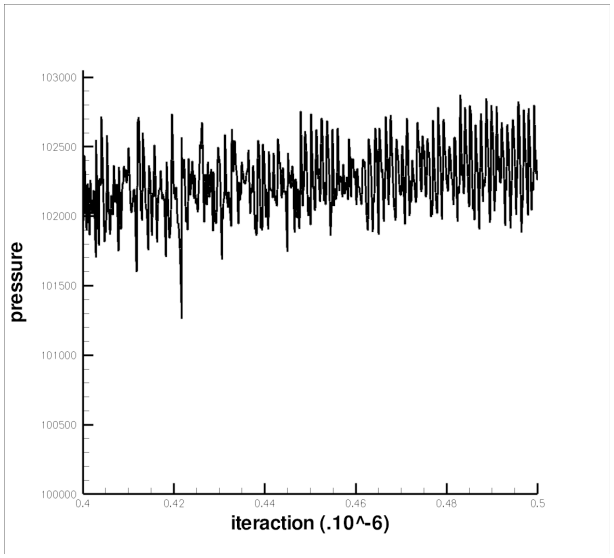

Figure 6.10: pressure probe above the airfoil for case2.

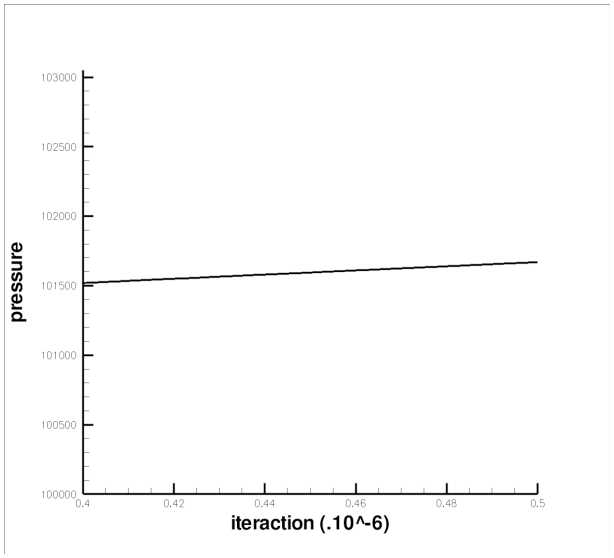

Figure 6.11: mean pressure probe above the airfoil for case2.

6.3 Time-Averaged Flow Solution with Divergent and Vorticity Sensors

In this section preliminary results for the new formulation of artificial viscosity are shown. These simulations were carried out to test the new sensor with the Euler solver. The values of $K^{(2)}_{\text{div}}$, $K^{(2)}_{\text{rot}}$ and $K^{(4)}$ used in this simulations suplies a first input to the linearized-euler solver. All the simulations are two-dimensional, Mach number igual 0.5 and one hundred elements along the airfoil chord, a 6x6 chords domain of regular cartesian mesh and a stretch zone of 200 elements in a rate of 1.05 in the directions +x, -x, +y and -y. Although the code performance was not affected by the new sensors implementation, there were no hardware disponibility to evalute 8x8 domain simulations.

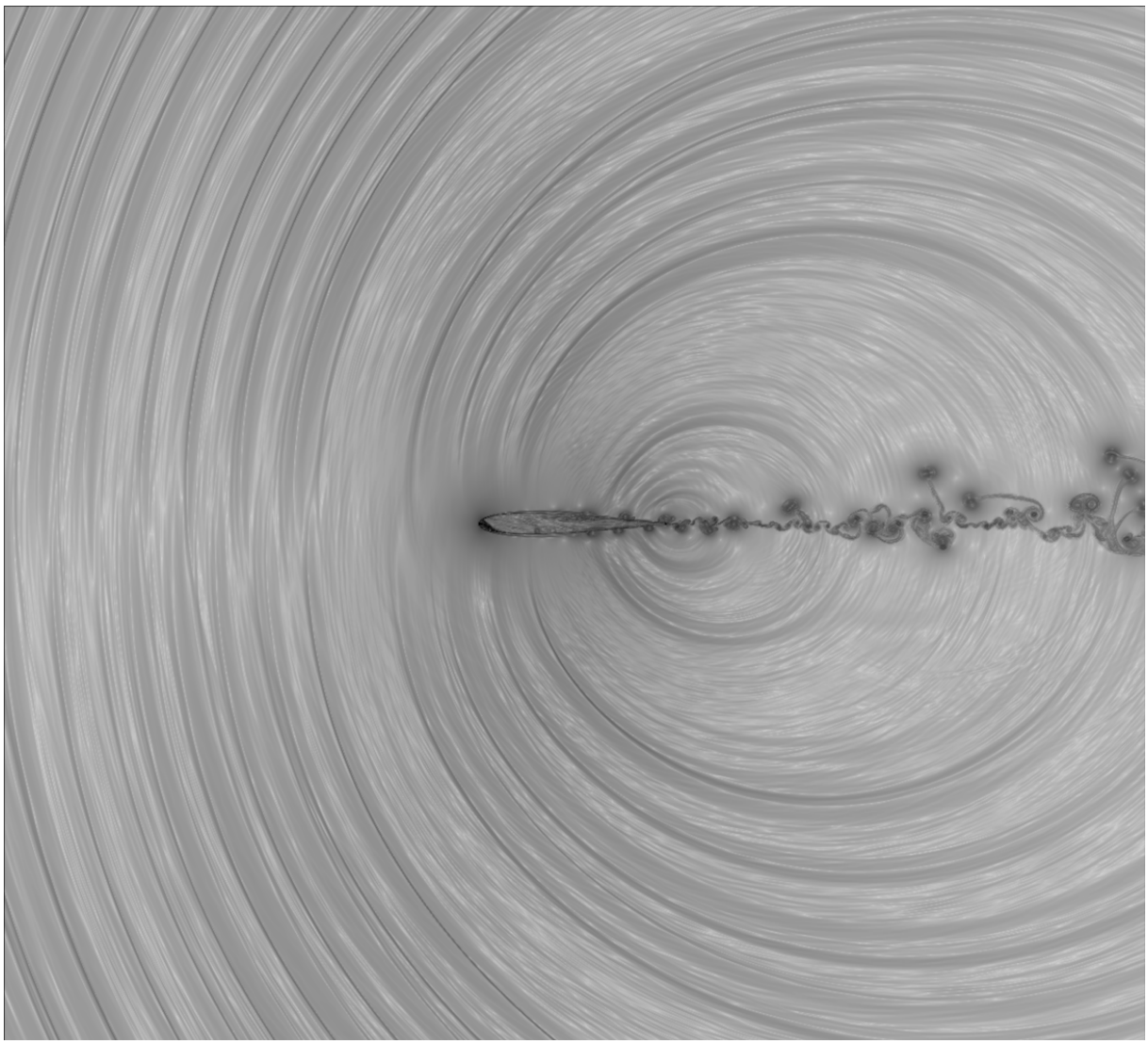

Figure 6.12: Unsteady flow solution for the nonlinear Euler equations for case1 with the new sensors implementation. The variable plotted is $\beta_T = |\nabla T|^{1/20}$.

Figure 6.12 shows a satisfatory aeroacoustic field. The sensors values used was: $K_{\text{div}}^{(2)} = 8.0x10^{-4}$, $K_{\text{rot}}^{(2)} = 2.0x10^{-5}$ and $K^{(4)} = 4.0x10 - 3$. A not expected result is noted in all Euler simulation. A stream spread is noted in the instantaneus field, figure 6.12, and in the mean field, figure 6.13. Although this unexpected stream the fisical meaning of the simulation does not seem to be afected since the c_p field still symetric, as shown in figure 6.13. The pressure distribuition on the airfoil surface corresponded to the expectations and the pressure probes in the mean field shows no oscilations as shown in figures 6.14 and 6.15.

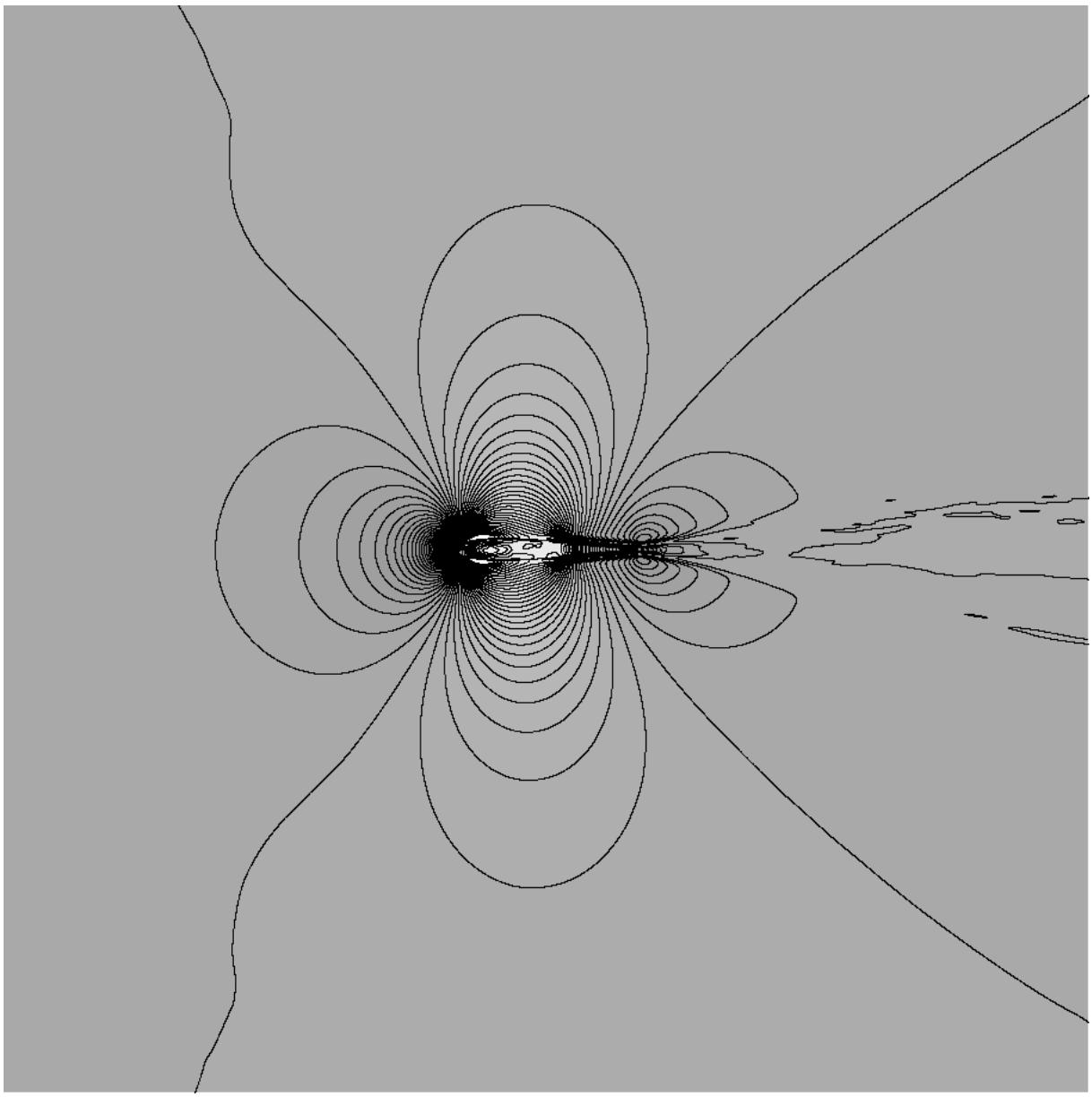

Figure 6.13: mean c_p field for case 1

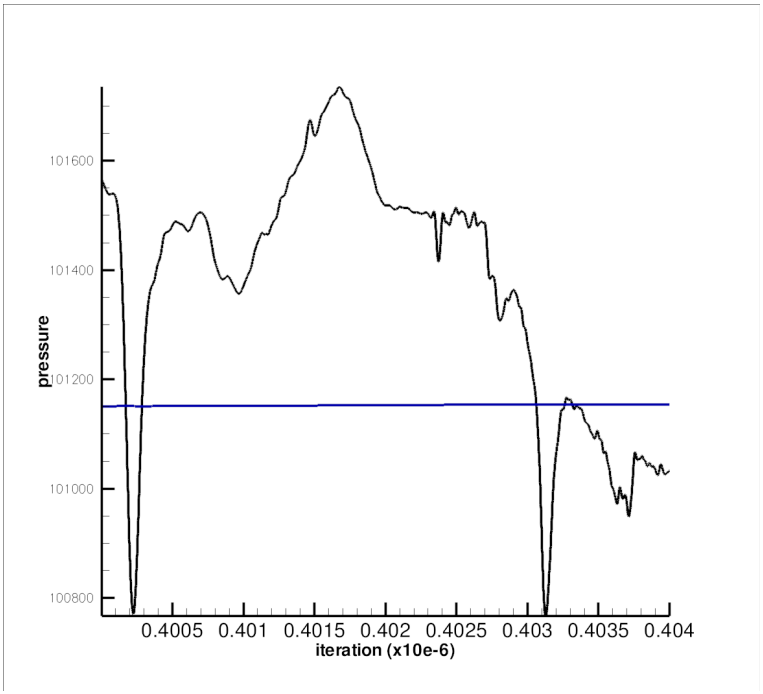

Figure 6.14: mean and instantaneus pressure probes localized under the airfoil for case 1

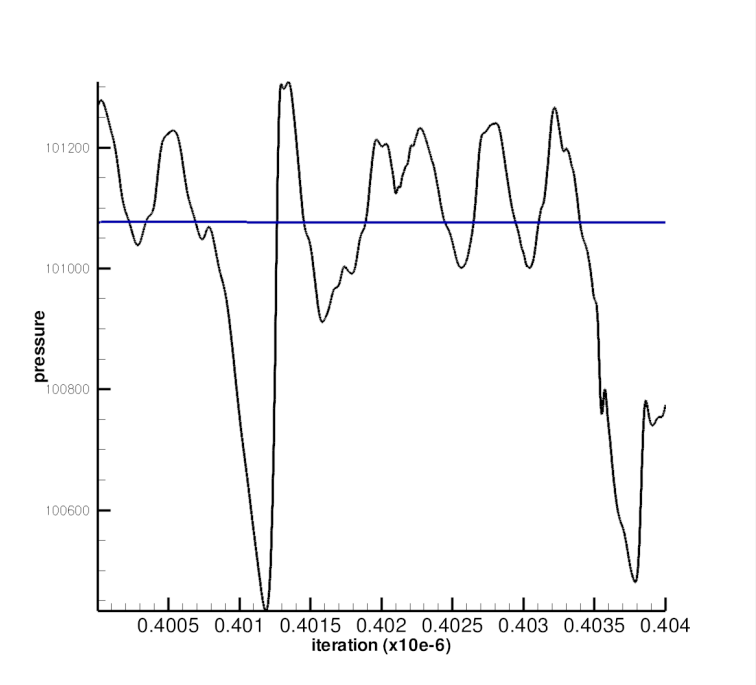

Figure 6.15: mean and instantaneus pressure probes localized in the stream for case 1

6.4 Linearized-euler Solutions

6.4.1 Vortical gust on uniform flow field

The first approach for the vortical gust implementation was by a time dependent acceleration, equations 4.4 and 4.5, imposed on the right-hand-side of the governing equations, eq. 5.24 and 5.25.

To evaluate the vortical gust implementation the gust was imposed in a uniform flow field. Mach number igual 0.5 and one hundred elements per length unit, a 1x1 domain of regular cartesian mesh and a stretch zone of 100 elements in a rate of 1.01 in the directions +x, -x, +y and -y.

Figure 6.16 shows the mean and instantaneus probes localized in the center of domain for uniform flow field for k=1.0. It shows a tendency to pressure mean (black line) to be a constant in $P = P_{\text{inf}}$. The instantaneus probe (blue line) shows a pressure response to a velocity variation in the domain as expected.

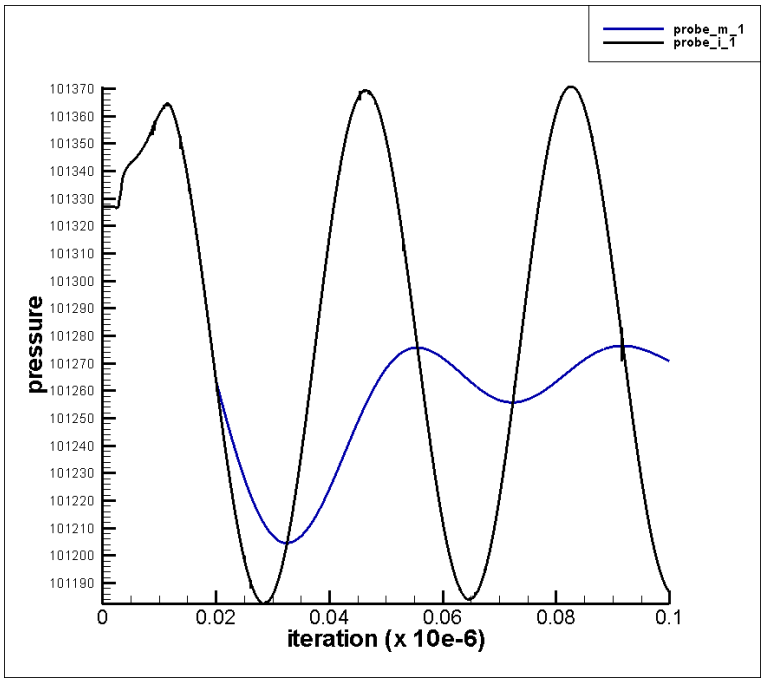

Figure 6.16: mean and instantaneus pressure probes localized in the center of domain for uniform flow field for k=1.0

With no boundary conditions the gust implementation went as expected, but combined with the immersed boundary condition undesirable results as floating point extrapolation.

Alternatively to the first approach, the time dependent velocity gust was imposed in a fixed y position upstream the airfoil in the regular domain as illustrated in fig. 6.17

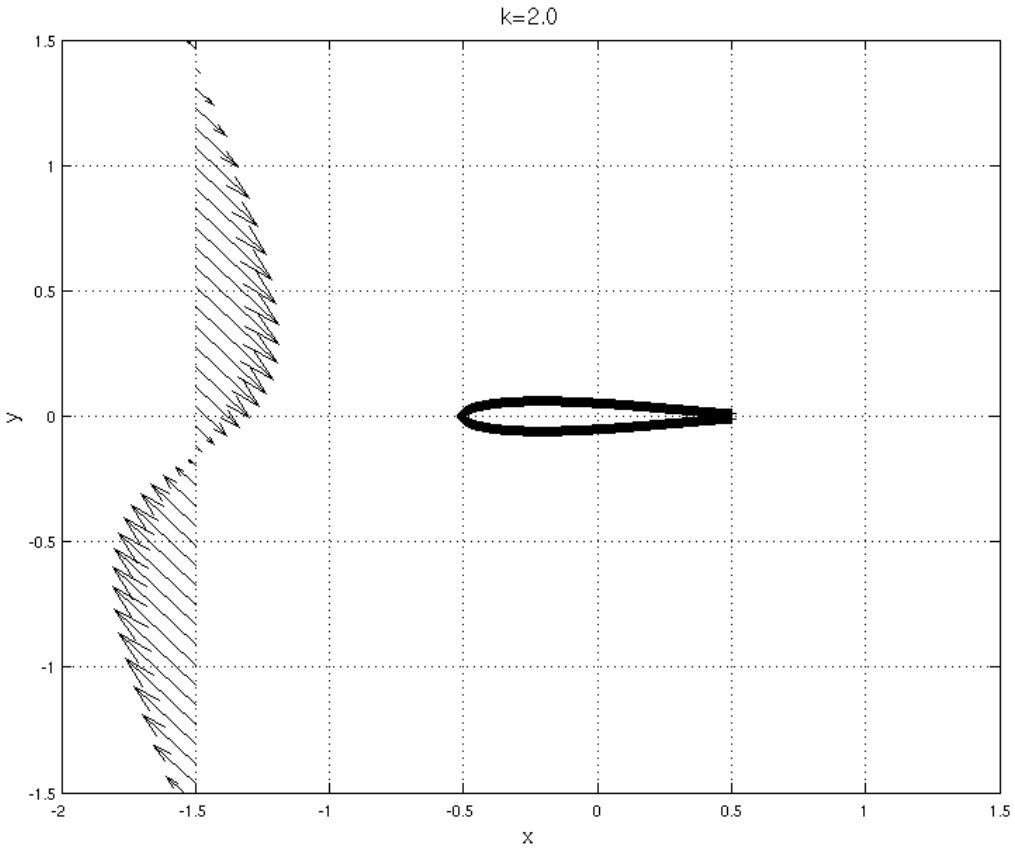

Figure 6.17: v' field for $k_x = k_y = 0.1$

In this approach the pressure response to the velocity imposition in the flow field was the same as in the first approach. Figure 6.18 show this pressure response for k=2.0.

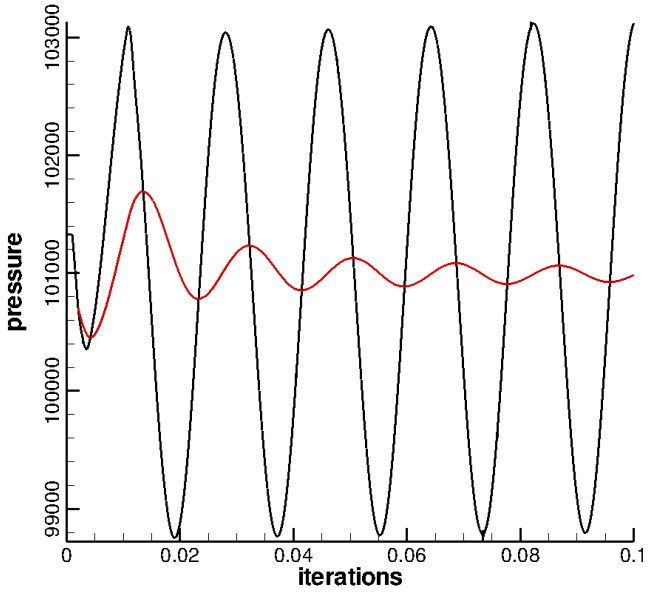

Figure 6.18: mean and instantaneus pressure probes localized in the center of domain for uniform flow field for k=2.0

6.4.2 Airfoil Gust Response

Figures 6.19, 6.20 and 6.21 show the v'_y field for k=2.0, 1.0 and 0.1 respectively in the regular domain 6x6.

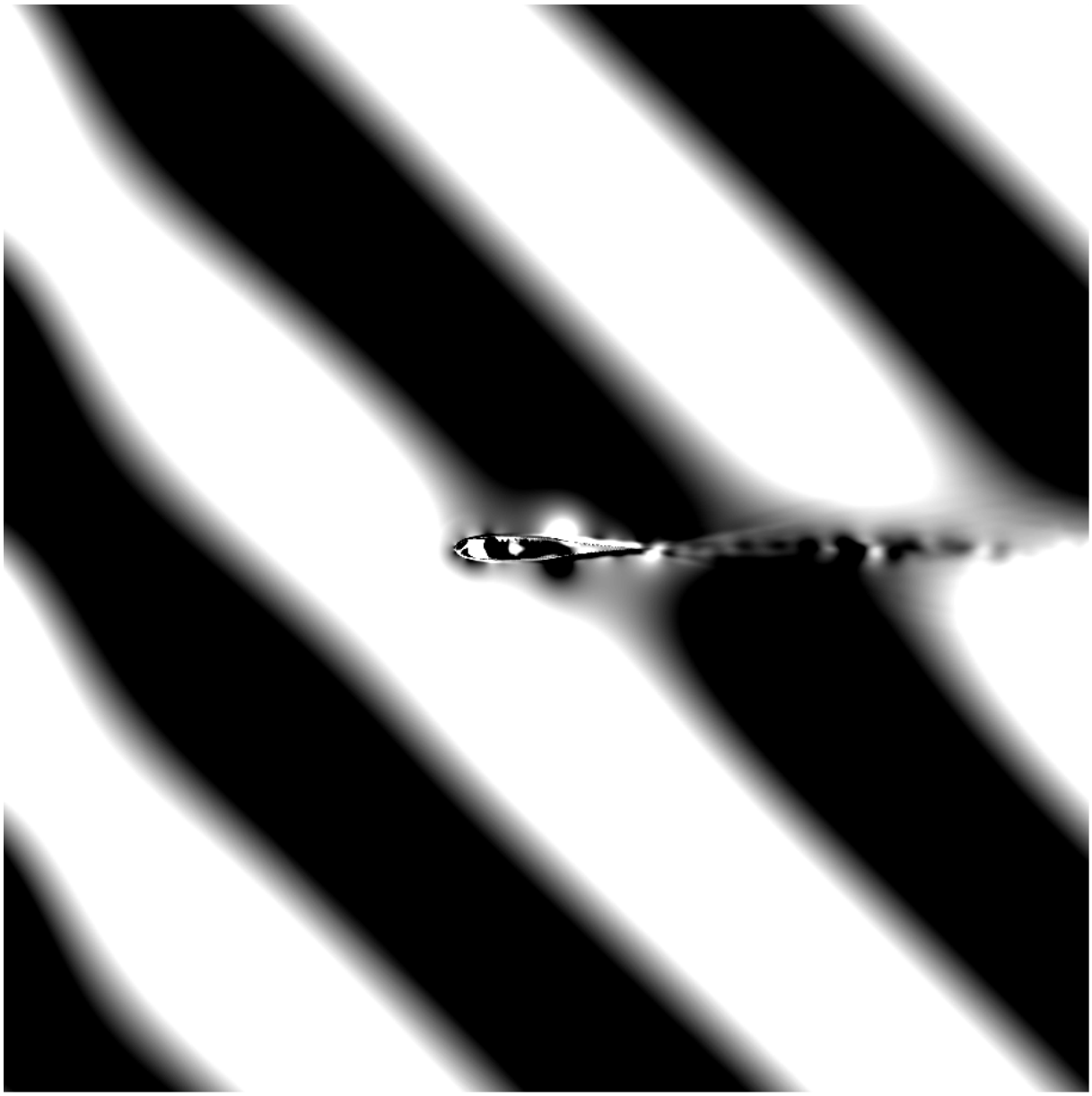

Figure 6.19: v' field for $k_x = k_y = 2.0$

Figure 6.20: v' field for $k_x = k_y = 1.0$

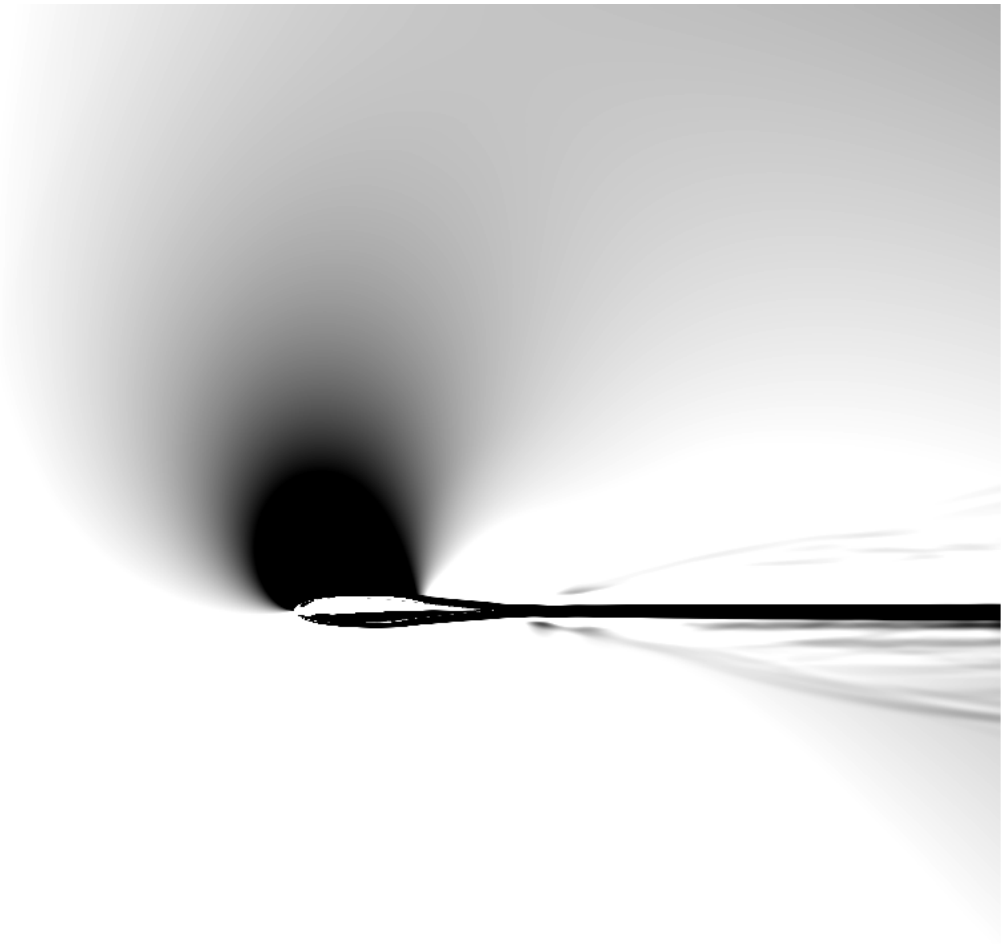

Figure 6.21: v' field for $k_x = k_y = 0.1$

Figures 6.24 to 6.27 present the acoustic intensity case 1 k=0.1, 1.0 and 2.0. The expected results are graphics with directivity of a dipole source.

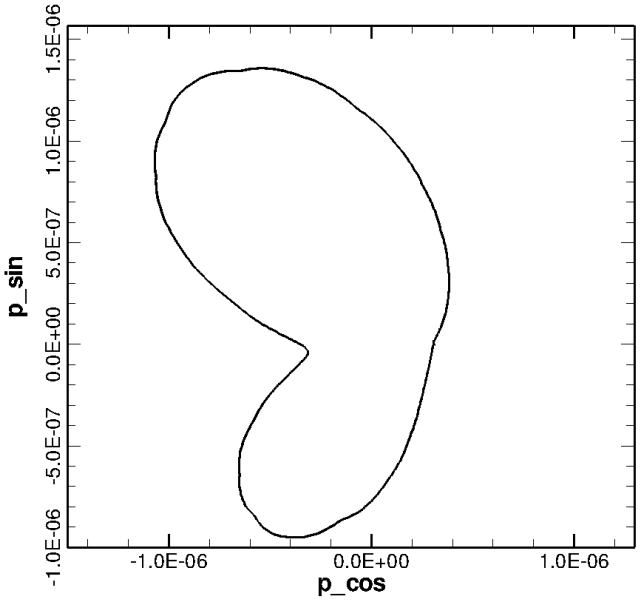

Figure 6.22: Acoustic intensity on circle $R = 1C$, Case 1, k=0.1

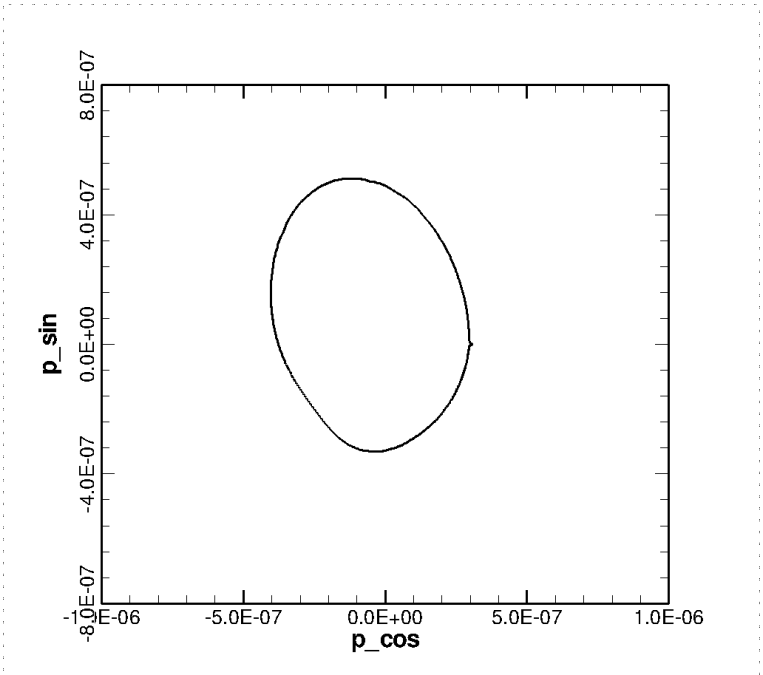

Figure 6.23: Acoustic intensity on circle $R = 2C$, Case 1, k=0.1

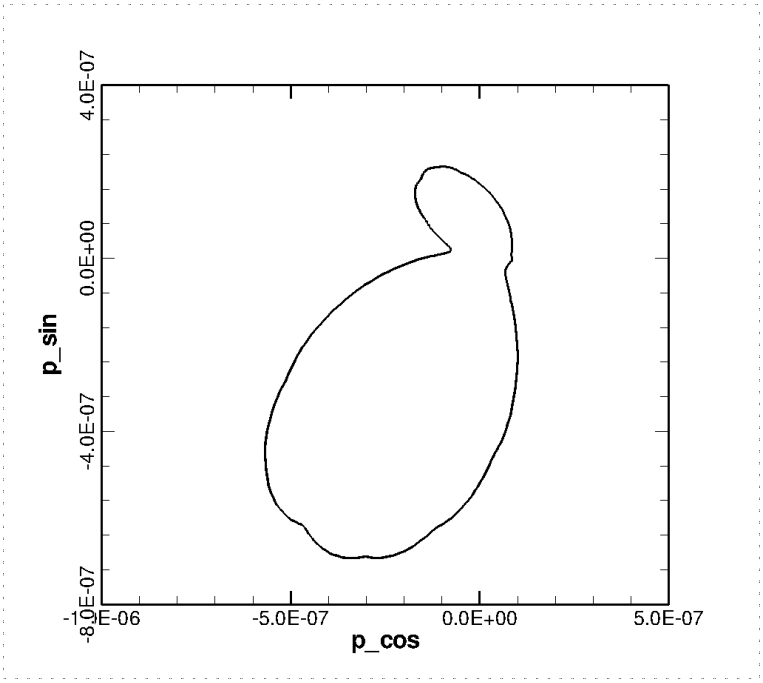

Figure 6.24: Acoustic intensity on circle $R = 1C$, Case 1, k=1.0

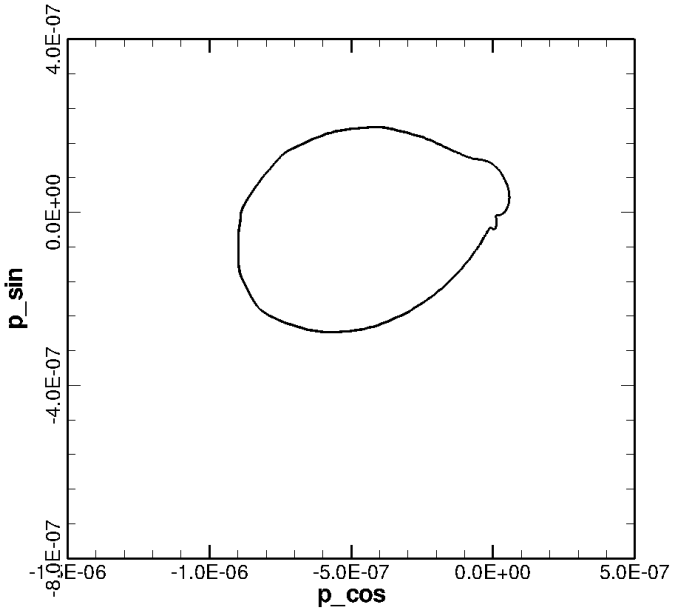

Figure 6.25: Acoustic intensity on circle $R = 2C$, Case 1, k=1.0

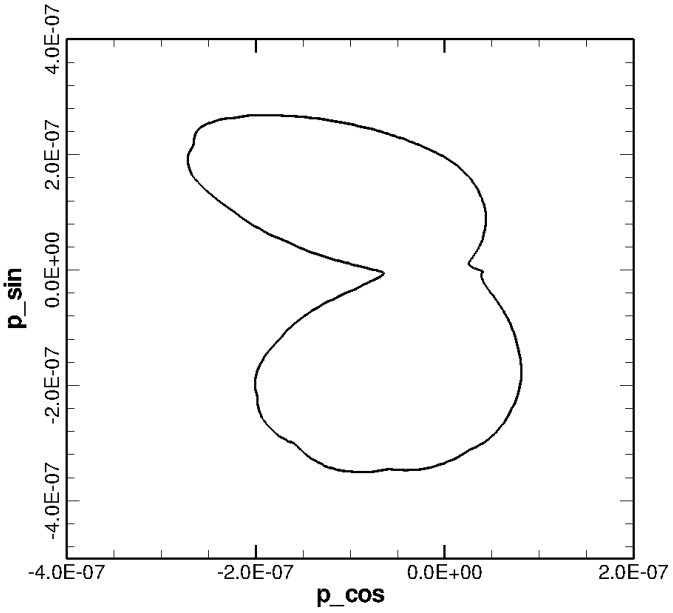

Figure 6.26: Acoustic intensity on circle $R = 1C$, Case 1, k=2.0

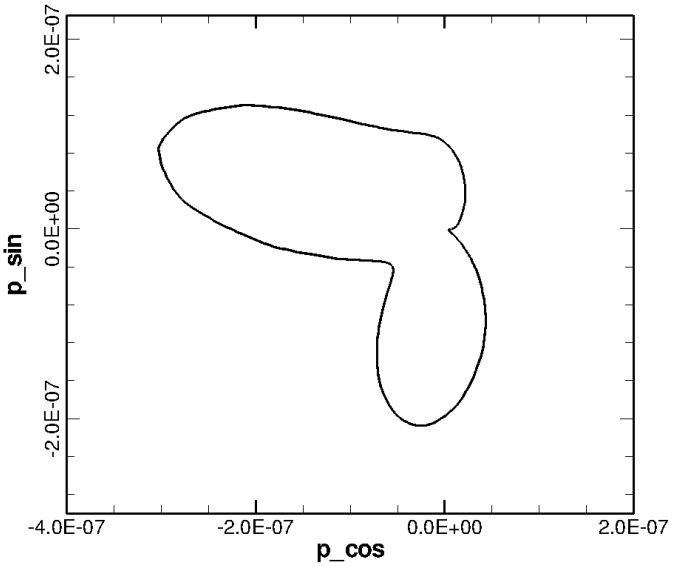

Figure 6.27: Acoustic intensity on circle $R = 2C$, Case 1, k=2.0

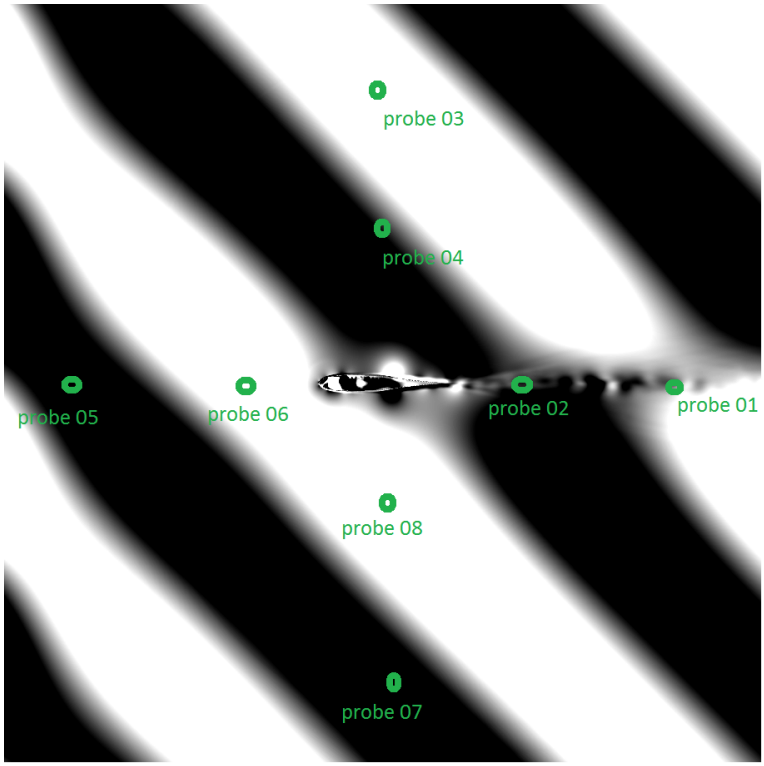

Figure 6.28: probe position

The directivity results are not as expected, altough the dipole caracteristics for the gust reponse are noted in the pressure probes located above and under the airfoil as shown in figure 6.29.

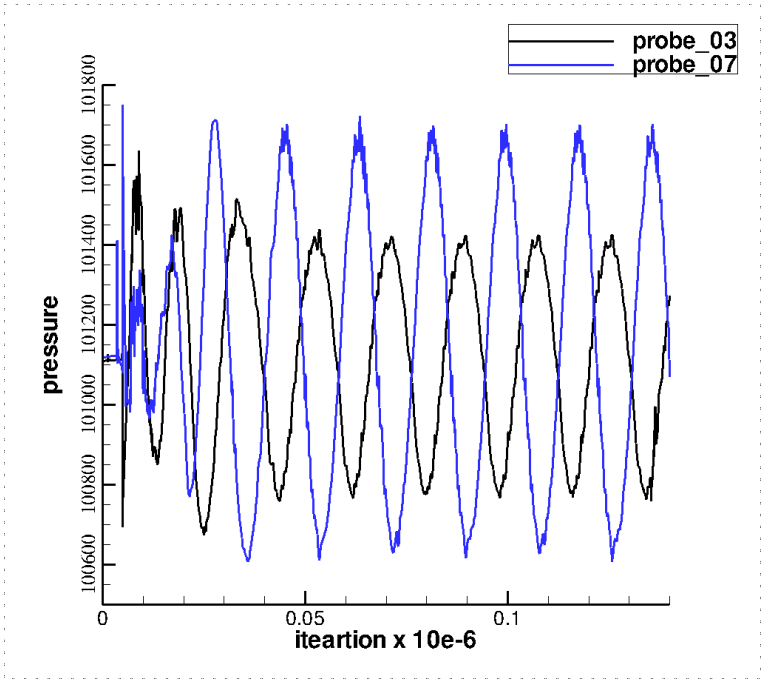

Figure 6.29: probes 03 and 07 pressure signal, Case 1, k=2.0

In Figure 6.30 the probes signal confirm the directivity graph shown in figure 6.27. The pressure variation is higher in probe 5 then in probe 3 as expected after the directivity graph.

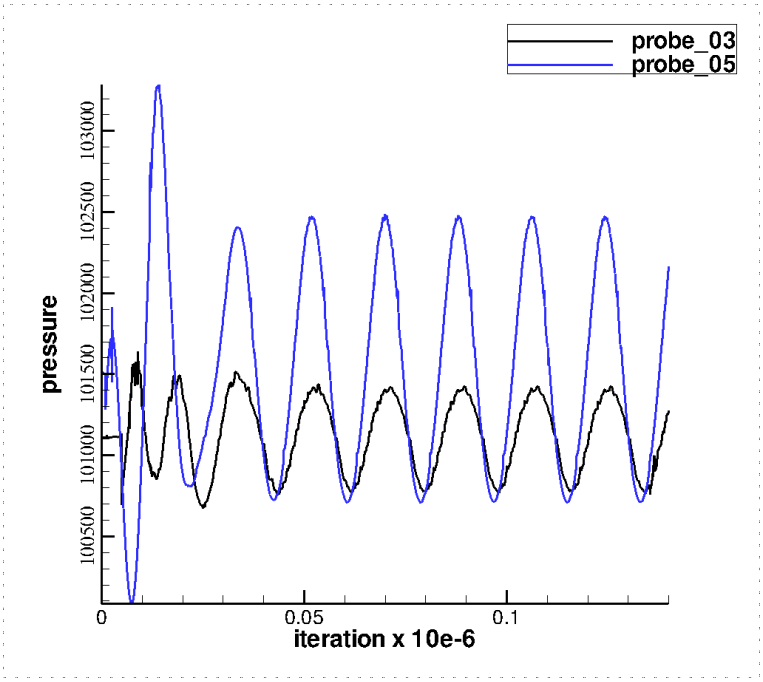

Figure 6.30: probes 03 and 05 pressure signal, Case 1, k=2.0

Figure 6.31 shows the pressure response in probe 03 for two different wave number. As expected, the response for a wave number two times higher (k=2.0) has twice the frequency of the response for k=1.0.

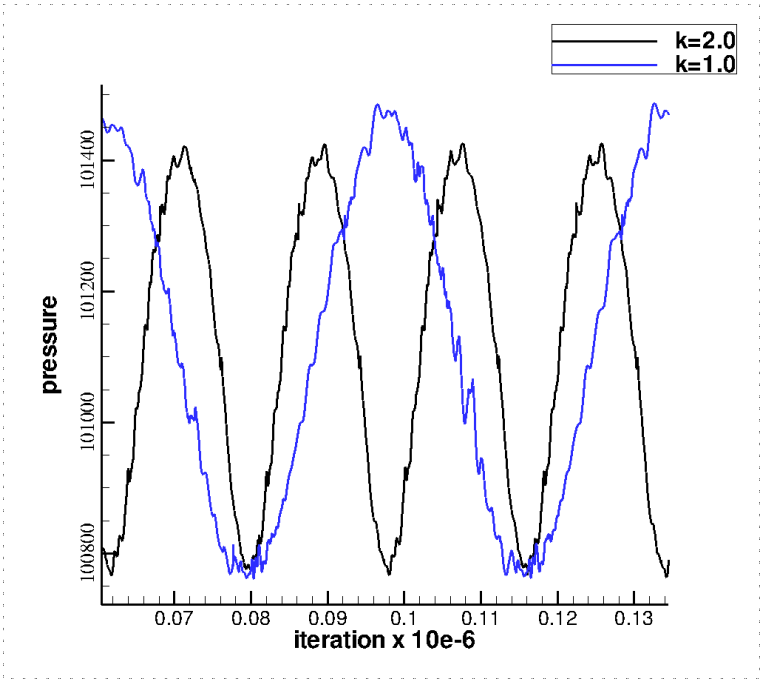

Figure 6.31: probes 03 pressure signal, Case 1, k=2.0 and k=1.0

7 CONCLUSION

The main objective of this work is the study of the self-induced noise produced on airfoils interacting with gust using the Virtual Aeroacoustic Tunnel (VAT). Comparisons between VAT results and GUST-3D, the NASA frequency-domain code, are shown in figures 6.23 and 6.25. Differences in the acoustic signals demonstrate some over dumping. This is probabily due to the artificial dissipation inherent of VAT code or some numeric dispearsion of the signal.

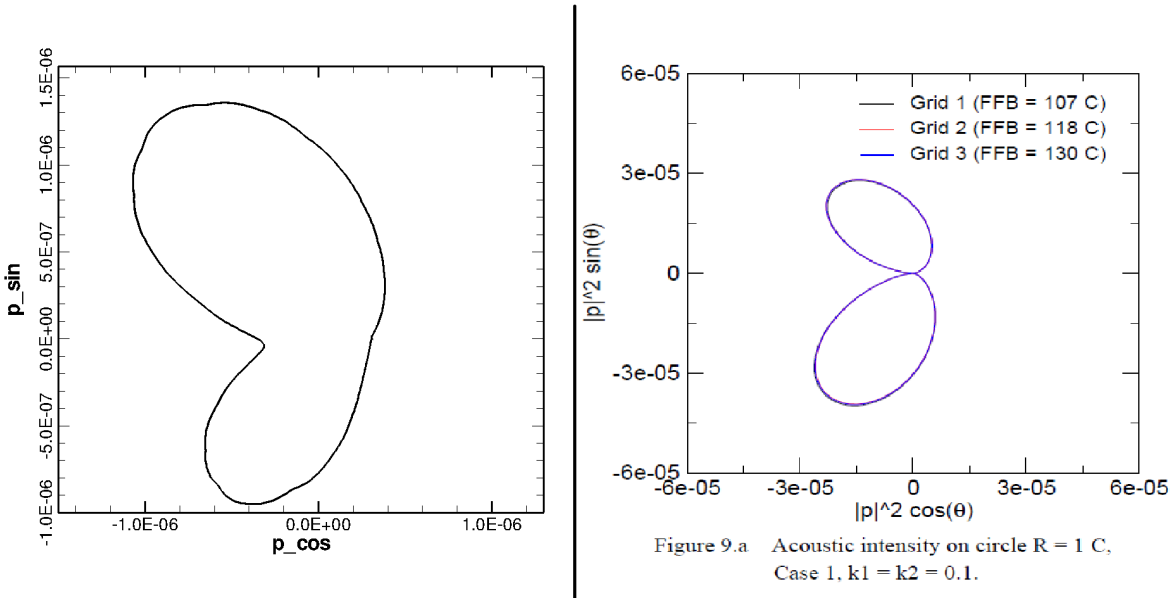

Figure 7.1: acoustic intensity comparation for case 1 k=0.1 r=1.0

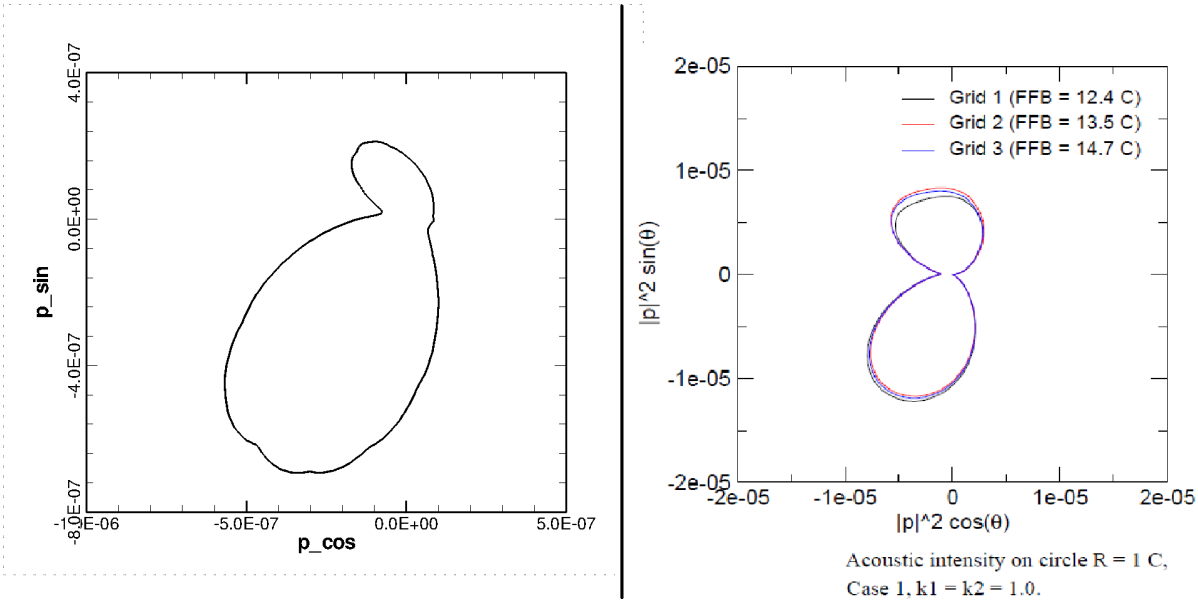

Figure 7.2: acoustic intensity comparation for case 1 k=1.0 r=1.0

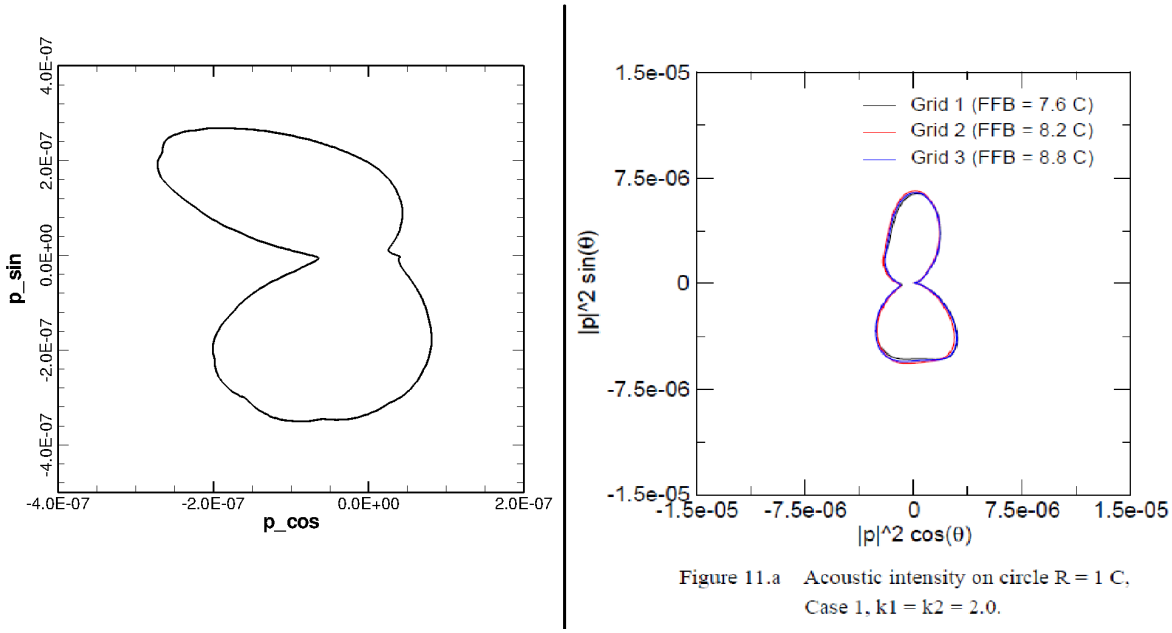

Figure 7.3: acoustic intensity comparation for case 1 k=2.0 r=1.0

Analyzing the frequency spectrum is possible to understand why the acoustic intensity gets so different. Figures 7.4 to 7.6 show the frequency spectrum for probe 03 for k=0.1, 1.0, 2.0 respectively. The broadband spectrum indicates that VAT code spreads the acoustic signal in multiple frequencies without a dominant tonal.

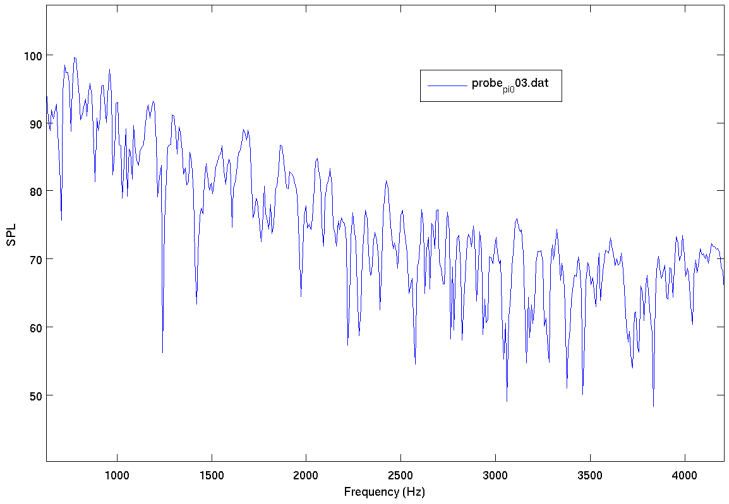

Figure 7.4: probes 03 frequency spectrum, Case 1, k=0.1

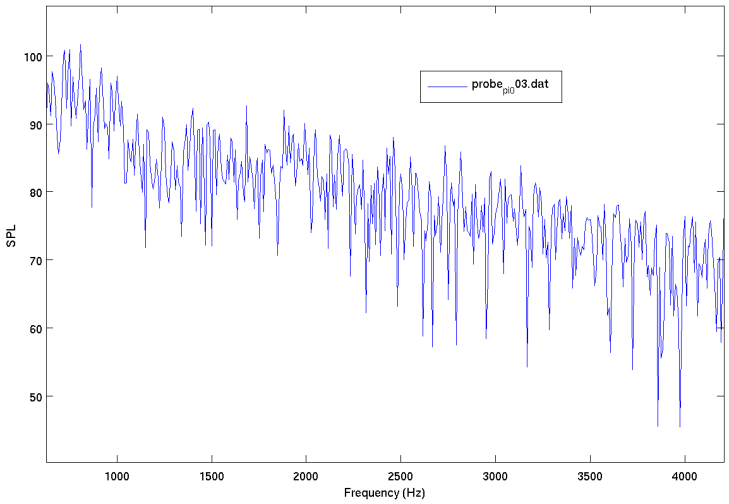

Figure 7.5: probes 03 frequency spectrum, Case 1, k=0.1

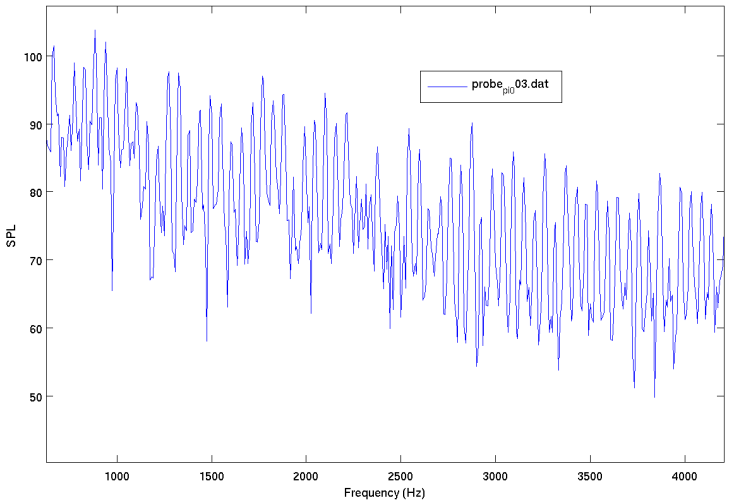

Figure 7.6: probes 03 frequency spectrum, Case 1, k=0.1

7.1 Next Steps

The following steps of the present work are:

1. Understanding this frequency spread and control it;
2. Solve the euler equations with different boundary conditions to evalute the mean field;
3. Solve the euler and the linearized euler equations for the asymmetric airfoil;
4. Compare the new results with the NASA "Fourth Computational Aeroacoustic Workshop on Benchmark Problems"

REFERENCES

http://environment.about.com/od/pollution/a/airport_noise.htm

ULF, Michel and HENRI, Siller, 2010, *Aircraft Noise Course*, Lecture Script, CLR IB 92517-09/B2,

DOBRZYNSKI, W., 2010, Almost 40 years of airframe noise research: What did we achieve?, Journal of Aircraft 47, 353-367.

CASPER, J., FARASSAT, F., 2002, *Trailing Edge Noise Prediction Based on a New Acoustic Formulation*, AIAA paper 2002-2477,

LARSSEN, J. D., DEVENPORT, W. J., 1999, *Acoustic Properties of the Virginia Tech Stability Wind Tunnel*, Rept. VPI-AOE-263, AOE Dept., Virginia Tech.

WANG, X., HIMANSU, A.,CHANG, S., JORGENSON, P., 2004, *Computation of a single airfoil gust reponse and gust-cascade interaction using the CD/SE method*, nasa/cp - 2004-212954

VLADIMIR, V., GOLUBEV, MANKBADI, R., 2004, *Space-Time Mapping Analysis of airfoil reponse to Impinging gust*, nasa/cp - 2004-212954

VLADIMIR, V., GOLUBEV, MANKBADI, R., HIXON, R., 2004, *Space-Time Mapping Analysis of airfoil reponse to Impinging gust using High-Order Prefactored Compact Code*, nasa/cp - 2004-212954

HIXON, R.,2003, *Space-Time Mapping Analysis for the Accurate Calculation of Complex Unsteady Flows*, AIAA paper 2003-3205, May 2003.

PATERSON, R.W., VOGT, P.G., and FINK, M.R., *Vortex noise of isolated airfoils*, AIAA Paper 72-656, 1972.

TAM, C.K.W., *Discrete tones of isolated airfoils*, J. Acoust. Soc. Am., 55(6):1173-1177, 1974.

CHONG, T.P. and JOSEPH, P., *An experimental study of tonal noise mechanism of laminar airfoils*, AIAA Paper 2009-3345. *In 15th AIAA/CEAS Aeroacoustics Conference*, 2009.

NASH, E.C., LOWSON, M.V. and McALPINE, A., *Noise genereted by airfoil profiles placed in a uniform laminar flow*, J. Fluid Mech., 382:27-61, 1999.

DESQUESNES, G., TERRACOL, M., and SAGAUT, P., *Numerical investigation of the tone noise mechanism over laminar airfoils*, J. Fluid Mech., 591:155-182, 2007.

ANDERSON, D. A., TANNEHILL, J. C., PLETCHER, R. H.,1983, *Computational Fluid Mechanics and Heat Transfer*, Hemisphe Publishing Corporation, 1st Ed., New York

ANDERSON, J.D. A.,1990, *Modern Compressible Flow*, McGraw-Hill Inc., 2nd ed., New York

Bobenrieth Miserda, R. F., de Mendonça, A. F., *Numerical Simulation of the Vortex-Shock Interactions in a Near-Base Laminar Flow*, 43rd AIAA Aerospace Sciences Meeting and Exhibit, AIAA-2005-0316, 2005.

Bobenrieth Miserda, R. F., Leal, R. G., *Numerical Simulation of the Unsteady Aerodynamic Forces over a Circular Cylinder in Transonic Flow*, 44th AIAA Aerospace Sciences Meeting and Exhibit, AIAA-2006-1408, 2006.

Bobenrieth Miserda, R. F., Jalowitzki, J. R., Lauterjung Q., R., *On the Effect of the Plunging and Pitching Motions over the Dynamic Response of an Airfoil in Transonic Laminar Flow*, 44th AIAA Aerospace Sciences Meeting and Exhibit, AIAA-2006-452, 2006.

Bobenrieth Miserda, R. F., Carvalho, A. G. F., *On the Effect of the Plunging Velocity over the Aerodynamic Forces for an Airfoil in Subsonic Laminar Flow*, 44th AIAA Aerospace Sciences Meeting and Exhibit, AIAA-2006-453, 2006.

Bobenrieth Miserda, R. F., Carvalho, A. G. F., *Direct Computation of the Noise Generated by Subsonic, Transonic, and Supersonic Cavity Flows*, 46th AIAA Aerospace Sciences Meeting and Exhibit, AIAA-2009-0008, 2008.

BOBENRIETH MISERDA, R.F., LAUTERJUNG, Q.R., MALDONADO, A.L.P., PAIVA, I., GODOY,K., NETO, O. *Direct Computation of Noise Generated by Complex Geometries Using a High-Order Immersed Boundary Method*, 15th AIAA/CEAS Aeroacoustics Conference, AIAA-2009-3181, 2009.

Bobenrieth Miserda, R. F., Maldonado, A. L. P., Gutierrez, B., *Simulation of the Cascade-Gust Interaction Problem Using a High-Order Immersed Boundary Method*, AIAA, 2009.

BROOKS, T. F., POPE, D. S. & Marcolini, M. A., (1989), *Airfoil self noise and prediction*, NASA Ref.Pub. 1218.

CRIVELLINI, A., GOLUBEV, V., MANKBADI, R., SCOTT, J., HIXON, R., POVINELLI, L., *Nonlinear analysis of airfoil high-intensity gust reponse using a high-order prefactored compact code*, AIAA paper, 2002.

DA CUNHA, D. A., 2009, *Simulacão numérica de ruído auto-induzido em bordo de fuga de aerofólio* , Graduation Project of Mechanical Engineering, University of Brasília, Brasília, DF, Brazil.

DUCROS, F., FERRAND, V.,NICOUD,F.,WEBER, C., DARRAQ, D., GACHERIEU, C.,POINSOT,T.,1999,*Large-Eddy Simulation of the Shock/Turbulence Interaction*, Journal of Computational Physics,152, 517-549.

DUCROS, F.,LAPORTE, F.,SOULÈRES, T., GUINOT, V., MOINAT, P., CARUELLE, B,2000, *High-Order Fluxes for Conservative Skew-Symmetric-like Schemes in Structured Meshes:Application to Compressible Flows*, Journal of Computational Physics, 161, 114-139.

HIRSCH, C.,2007, *Numerical Computation of Internal and External Flows*, Elsevier, 1st Volume, 2nd Edition.

JAMESON, A., SCHMIDT, W., TURKEL, E.,1981, *Numerical Solutions of the Euler Equations by Finite Volume Methods Using Runge-Kutta Time-Stepping Schemes*, AIAA 14th Fluid and Plasma Dynamics Conference, AIAA-81-1259, Palo Alto, California.

MALDONADO, A. L., CARMO, I. L., 2008, *Cômputo direto do ruído gerado por escoamento ao redor do cilindro*, Graduation Project of Mechanical Engineering, University of Brasília, Brasília, DF, Brazil.

MISERDA, R. F. B., QUEIROZ R. L., MALDONADO, A. L., RIBEIRO I. D., GODOY, K., NETO, O. G., 2009, *Direct computation of noise generated by complex geometries using a high-order immersed boundary method*

MITTAL, R., IACCARINO, G., 2005, *Immersed Boudary Methods.*, Annu. Rev. Fluid Mech.

Fourth Computational Aeroacoustics (CAA) Workshop on Benchmark Problems, NASA-CP-2004-212954, 2004.

PIMENTA, B. G., VIZIOLI, T. R., 2009, *Numerical simulation of noise generated by the flow over rotor cascades*, Graduation Project of Mechanical Engineering, University of Brasília, Brasília, DF, Brazil.

SCOTT, James R., 2004, *Category 3 problem 1 - Single Airfoil Gust Response*, NASA/CP-2004-212954

YEE, H. C.,1997,*Explicit and Implicit Multidimensional Compact High-Resolution Shock-Capturing Methods: Formulation*,Journal of Computational Physics,131,216-232.